



저작자표시-비영리-변경금지 2.0 대한민국

이용자는 아래의 조건을 따르는 경우에 한하여 자유롭게

- 이 저작물을 복제, 배포, 전송, 전시, 공연 및 방송할 수 있습니다.

다음과 같은 조건을 따라야 합니다:



저작자표시. 귀하는 원저작자를 표시하여야 합니다.



비영리. 귀하는 이 저작물을 영리 목적으로 이용할 수 없습니다.



변경금지. 귀하는 이 저작물을 개작, 변형 또는 가공할 수 없습니다.

- 귀하는, 이 저작물의 재이용이나 배포의 경우, 이 저작물에 적용된 이용허락조건을 명확하게 나타내어야 합니다.
- 저작권자로부터 별도의 허가를 받으면 이러한 조건들은 적용되지 않습니다.

저작권법에 따른 이용자의 권리는 위의 내용에 의하여 영향을 받지 않습니다.

이것은 [이용허락규약\(Legal Code\)](#)을 이해하기 쉽게 요약한 것입니다.

[Disclaimer](#)

이학박사 학위논문

기계적 벤딩과 광학 트위징 이용한
테라헤르츠 나노안테나
광학적 반응 측정

Connectivity-changing terahertz nanoantennas
manipulated
by mechanical bending and optical tweezing

2021년 8월

서울대학교 대학원

물리천문학부

이 지 예

기계적 벤딩과 광학 트위징 이용한
테라헤르츠 나노안테나
광학적 반응 측정

지도교수 홍 성 철

이 논문을 이학박사 학위논문으로 제출함
2021년 8월

서울대학교 대학원
물리천문학부
이 지 예

이지예의 이학박사 학위논문을 인준함
2021년 8월

위 원 장 전 현 수

부위원장 홍 성 철

위 원 홍 승 훈

위 원 이 규 철

위 원 박 영 미

Abstract

Resonators with metallic nanometer gap structures are used and aimed for controlling the enhanced and the local confinement of the electromagnetic waves funneling through the metallic gaps of the resonators. Studies showed that the active resonators manipulate one of the optical responses, for instance, the amplitude, and the resonance frequency of the incident electromagnetic waves, by changing the connectivity of the gap of the resonators. In this work, we changed the connectivity of the gaps based on terahertz bowtie antennas and observed the optical responses on the terahertz spectrum. First, we fabricated a two-fold terahertz resonator where bending the flexible substrate outward breaks a diabolo array into a bowtie array. For the cases on flattening/ bending/ re-flattening, the electrical properties in conductance measurements and optical properties in THz transmission spectra are analyzed. While the conductance shows electrically connected in the diabolo antennas and

disconnected in bowtie antennas results, THz transmittance shows two-fold resonant behavior. In this manner, we drop-casted lactose and caffeine molecules on the resonator, respectively. When the absorption peak of the chemicals and the resonant frequency match, the chemical sensing properties show increased sensitivity and selectivity compared to drop-casting on a bare substrate. On the other hand, we conducted a single particle detection experiment by putting the particle in a single bowtie nanogap with optical tweezing and detect it in a terahertz reflection spectrum. We found the conditions for stably manipulating a single particle by optical tweezing and analyzed it with trapping video, confirming that the size of the trapping potential is four times greater than the Brownian motion ($1 k_B T \sim 26 \text{ meV}$). The reduced amplitude in terahertz reflectance was observed by terahertz time-domain spectroscopy, and the simulation results ensured that a single gold particle filled the bowtie gap. These works will open up as a preliminary step in the detection of single or multiple biomolecules, providing practical applications.

Keywords: terahertz time-domain spectroscopy, terahertz bowtie nanoantenna, flexible, optical tweezing, terahertz modulation, molecule sensing

Student Number: 2013-30119

Table of Contents

Chapter 1. Introduction.....	1
Chapter 2. Connectivity-changing resonator by mechanical bending.....	5
2.1 Introduction.....	5
2.2 Preparation of break-junction based bowtie array.....	9
2.3 Transmission-type THz time-domain spectroscopy.....	15
2.4 Two-fold resonant behavior.....	17
2.5 Chemical sensing experiment.....	30
Chapter 3. Connectivity-changing resonator by optical tweezing.....	40
3.1 Introduction.....	40
3.2 Preparation of a single bowtie antenna chip and gold nanoparticles	42
3.3 Top-down optical tweezing THz probe system.....	45
3.4 Stabalized optical tweezing conditions.....	50
3.5 A single gold nanoparticle detection in THz reflection spectrum	56
Chapter 4. Conclusion.....	59
Appendix.....	61
Bibliography.....	63
Abstract in Korean.....	78

Chapter 1.

Introduction

Nanometer-gap structures are widespread in nanoplasmonics including nanoantennas [1,2], which can be applied to surface-enhanced Raman scattering (SERS) sensing [3,4], biomaterial sensing [5,6], non-linear behaviors [7,8], optical circuits [9], and optical trappings [10,11]. From visible lights to gigahertz waves, studies have shown that light waves can funnel through a nanometer-gap enhancing electromagnetic fields [12-17].

Controlling the enhanced and the local confinement of the electromagnetic waves funneling through the metallic gaps was the key to develop their optical devices. Recently, ‘active’ resonators are introduced for manipulating one of the optical responses, for instance, the phase [18], the amplitude [19], and the resonance frequency of the incident electromagnetic waves [20]. These researchers integrated the external control

systems on their passive counterparts to tune the optical properties likewise by applying the gate voltage [21,22] or adjusting the optical pump intensity [23], and/or changing the temperature of the active dielectric material [24]. However, when it comes to flexible substrates, resonators through mechanical deformation showed frequency tunability without applying additional control pads or complex configurations for operation. Stretchable resonators show broad tunability, however it had limited tensile strains for preventing the distortion of the metallic patterns on the substrate [25-29].

Here, we fabricated a metallic diabolo array by e-beam lithography on a polyethylene terephthalate (PET) substrate without an additional controlling system. We distorted the diabolo array to bowtie array by bending it outward. After flattening it again, the array is restored to a diabolo array and confirmed by the THz transmission spectra of when the sample was flat before/after bending. While the electrical characteristics of those two cases show electrically-connected and -disconnected in conductance measurement, the THz resonator is switchable and show two-fold resonator behavior

from a THz spectroscopic view. Therefore, we detected two different chemicals that correlate the resonant frequency of diabolos and bowties, respectively.

On the other hand, there has been growing interest to explore optimal methods for the manipulation of small particles, since they provide clear benefits of non-contact and low perturbation [30-34]. The most representative method is an optical tweezer, which traps particles at the dipole force minima. Since the terahertz waves show low photon energy (4.1 meV at 1 THz), it is hard to trap the single particle at room temperature (26 meV at 300 K). However, the intra- and inter-molecular vibrational modes lie in the THz frequency range which is good for sensing chemicals. Therefore, if the target chemical is labeled on a single gold nanoparticle, the chemical can be detected by THz antenna. In specific, if the nanoparticle fills in the particle-sized gap of bowtie antenna, then the optical response in the THz spectrum will change.

Here, we change the connectivity of the bowtie nanogap antenna putting or removing the gap-sized nanoparticle by optical tweezing, and observe the corresponding THz

reflection amplitudes in THz spectrum. First, we ensure that the optical tweezing setup is stabilized to manipulate a 400 nm-sized-gold nanoparticle by the trapping video. The extracted the distributions of the particles were much smaller than the diffraction limit of the trapping laser beam, and also the amplitude of the trapping potential from the experiment showed four times higher than the thermal energy at room temperature. The top-down optical tweezing THz-probe system enabled to detect a particle in THz spectrum while optical tweezing a particle in the gap at the same time. We observed a decrease of the reflection amplitude while the metallic particle connected the bowtie gap.

Chapter 2.

Connectivity—changing resonator by mechanical bending

2.1. Introduction

Active resonators are mainly for manipulating one of the optical responses, as mentioned in chapter 1. Despite the achievement, the approaches need extra space and/or fabrication process to control pads or control systems, which must be further improved. In the light, stretching can be a candidate to overcome the complicated structure and fabrication process. Indeed, stretchable resonators have been reported, where broad tenability is accomplished with tensile strain [25-27]. However, the strain range is not broadened enough in frequency domain to prevent metallic pad from being distorted, limiting versatile operations [28,29].

The other way to make active flexible optical antennas is to bend the substrate and break the metallic notched bridge structures. For instance, previous studies broke the middle part of the diabolo-shaped electrode and made an air gap via a mechanically controllable break junction (MCBC) [35,36]. The motorized rod moves vertical and pushes gently from the bottom of the substrate where the notched bridge part exists while two counter supports are fixed in position at a lateral distance. The rod pushes until the metallic rod elongates and break, eventually an air gap appears in between the metallic electrodes. The gap width of the metallic electrodes is controllable by bending the substrate. Although this can be suitable for generating a few nanometer-gap antennas [37,38], this method allows one nanometer-gap for a discrete sample at once. Some researchers tried to fabricate antenna arrays over large areas in different methods, such as electromigration [39] and crack-defined break junctions (CDBJ) [40]. The former requires additional electrode pads. The latter requires a silicon-titanium nitride (Si/TiN) layer and an etching process to strain the metallic electrode, resulting in at least two-step

lithography. A suitable design for these methods is narrowed for stripes and rods, not for discrete antenna arrays, and the fabrication yield for the large area is not solved yet. In specific, Dubois et al. reported that the fabrication densities reached as high as 7 million junctions per cm^2 , where the nanometer-gap yields of around 7%.

Here, we applied the mechanical bending method to create the array of metal nanogap embedded in THz resonator with millimetre scale of sample area for THz studies such as THz responses and sensing applications. Our break junction-based two-fold THz resonator composed of the gap-closable bowtie array covers millimetre-scale, allowing chip-scale patterned modulators. Although there are representatives, e.g., electrically controlled MEMS (microelectromechanical systems) switches [41] and stretchable metamaterials [42] reported recently, however no two-fold resonance shift-able chip-scale array is introduced in THz fields yet. We fabricated a metallic diabolo array on a flexible commercial substrate. The entire diabolo array broke into a bowtie array by bending it outward, generating a two-fold resonator. After flattening

the substrate again, the array changed back to a diabolo array showing that the antenna's resonance is recovered without any additional controlling system. The electric-field distributions depending on bending radius are shown to find the relation between the antenna's shape and its resonance frequency. For the patterned/bent/flattened-again case, the current-voltage characteristics were all different. However, the THz resonator is switchable and reproducible from a THz spectroscopic view. The two-foldable resonator is applied to detect distinct molecules, lactose and caffeine powder. Each resonant absorption corresponding to the bowtie and diabolo array is obtained by mechanical bending and flattening. Regarding the resonance-tuning modulation bandwidth and the sensing transmission spectrum performance with sub-millimeter waves, the chip-scaled resonator can be obtained time-efficiently even with a break-induced antenna array not elaborated. Therefore, we expect that this concept for mechanical two-fold tenability can be extended for detecting various chemical-, and bio-molecules in THz sensing device applications.

2.2. Preparation of break-junction based bowtie array

Figure 2.1 presents a structure of a two-fold plasmonic resonator and the operation in THz transmission. A diabolo array is fabricated on a flexible PET substrate by electron-beam lithography. As we bend the flat resonator outward (Hereafter, it is called bending.) with radius, $R = 8$ mm, the narrowest part of the metallic diabolo is broken and changed into a bowtie array with the gap width of 650 nm (Figure 2.2b). Even though it is difficult to control the exact position of break-junction, we observed that the narrowest part is most preferred for the gap formation. The narrower metallic constriction, the more effective tensile stress is applied, and consequently, break-junction is achieved (Figure 2.3). As the shape of the resonator changes from the diabolo array to the bowtie array by bending, the corresponding resonance frequencies in THz transmission spectra changes from 0.5 THz to 1.1 THz. We note that the variations of gap position

and size do not significantly affect the terahertz transmission spectrum because of millimeter wavelengths of THz waves (See Figure 2.4). As we release the bending and flatten the entire substrate, the bowtie array gaps are closed and the shape returns as the diabolo array and the resonance frequency shifts back to 0.5 THz, operating as a two-fold frequency shift resonator (Figure 2.2c, and 2.4d-e).

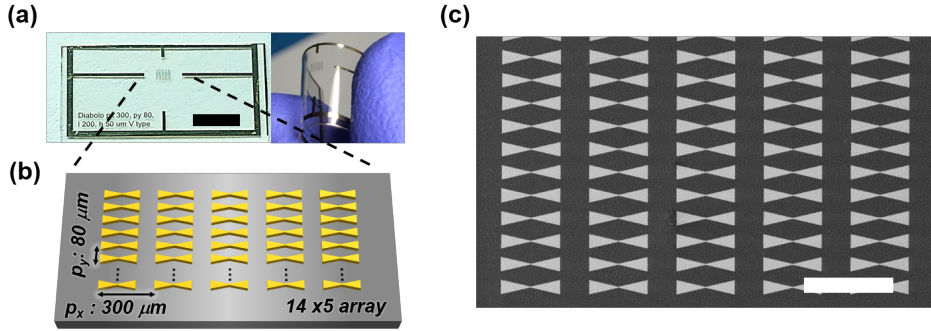


Figure 2.1. Preparation of a two-fold THz resonator on a bendable substrate. (a) Photographs of a THz resonator fabricated on a PET substrate in flat (left) and in bent condition (right). A schematic (b) and the corresponding SEM image (c) of a diablo array on a flexible substrate. Scale bars: (a) 5 mm; (c) 300 μm .

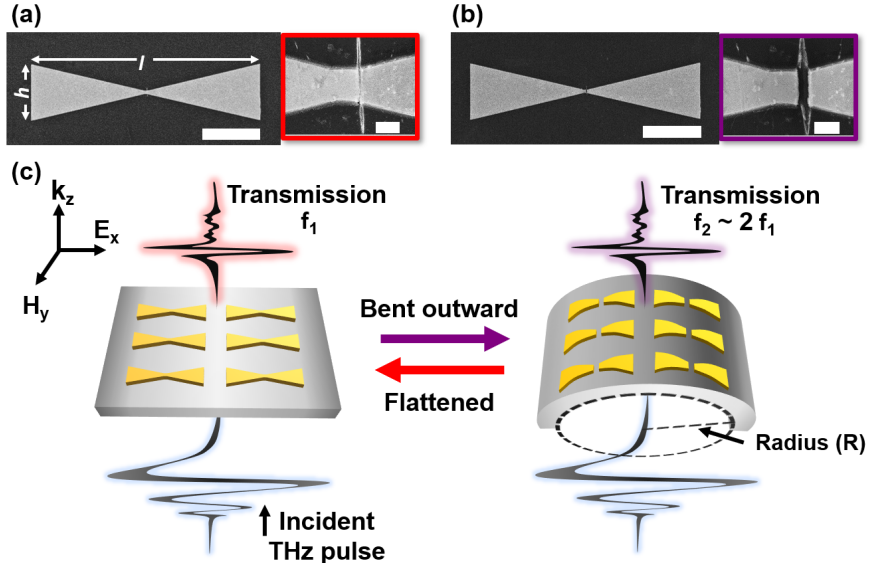


Figure 2.2. Operation of a two-fold THz resonator on a bendable substrate. Enlarged SEM images of the resonator (a) in flat and (b) in bent condition, where length and edge-width are denoted as l and h , respectively. Further zoomed-in-images marked by red (a) and purple (b) box show that a diabolo array breaks into the bowtie array in bent condition. (c) Schematic diagrams of THz transmission through the two-fold THz resonator in the case of (a) and (b) which exhibit representative resonance

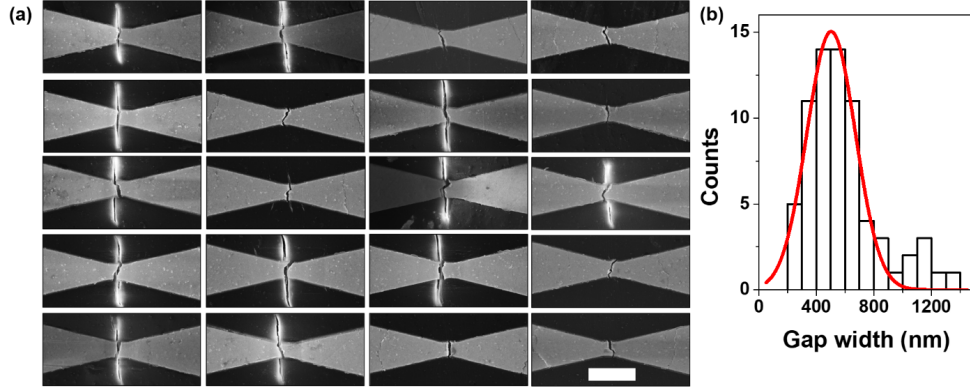


Figure 2.3. Gap-width and gap-position of bowtie antenna array as a two-fold resonator at bending radius $R = 8$ mm. (a) Representative SEM images of bowtie antennas (the total length of $200\ \mu\text{m}$) near the gap at $R = 8$ mm for 14 by 5 array (total 70) sample. Scale bar for the images is $5\ \mu\text{m}$. (b) Statistical histogram of the 70 - bowtie antennas' gap width from a two-fold resonator. The red line denotes Gaussian distribution fitting curve, based on the average gap width $503\ \text{nm}$ and the standard deviation $169\ \text{nm}$ that are extracted from the histogram.

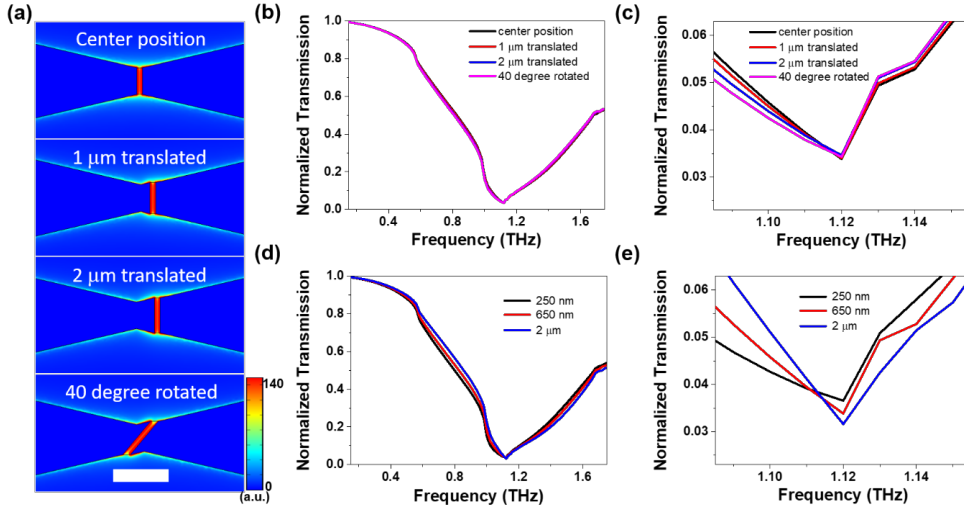


Figure 2.4. Gap randomness and its THz transmission spectra of the two-fold resonator at bending radius $R = 8$ mm. (a) Electric-field distributions for four different gap positions with 500 nm gap width calculated by COMSOL simulation. Scale bar for the images is 5 μm . (b-c) Corresponding terahertz transmission spectra (b) and enlarged graph (c). The resonance frequencies are located around 1.12 THz. (d-e) Calculated THz transmission spectra (d) and enlarged version (e) for three different gap widths (250 nm, 650 nm, and 2 μm) of the bowtie antennas where the gaps are formed at the diablo center. The resonance frequencies are gathered around at 1.12 THz.

2.3. Transmission-type THz time-domain spectroscopy

We used electro-optic sampling terahertz time-domain spectroscopy (THz-TDS) for THz transmission measurements of a two-fold plasmonic resonator. A femtosecond Ti:sapphire laser with a repetition rate of 80 MHz is illuminated on a biased low-temperature grown gallium arsenide (LT-GaAs) emitter to generate THz pulses. These pulses are normally incident on a center of the resonator substrate. A flat- and a radius of 8 mm curved- 2 mm \times 2 mm punched aluminium aperture are designed to define the transmission area. For instance, when the resonator is attached on the flat (8 mm curved) version of aperture, the pulse first transmits the aperture and then transmit the PET substrate of the diabolo (bowtie) array. The transmitted THz waves are collected by parabolic mirrors and detected by a zinc telluride (ZnTe) crystal in electro-optic sampling method. These pulses in time domain signals are Fourier transformed into frequency domain which shows THz transmission spectrum. The humidity of the sample loading chamber was 9%.

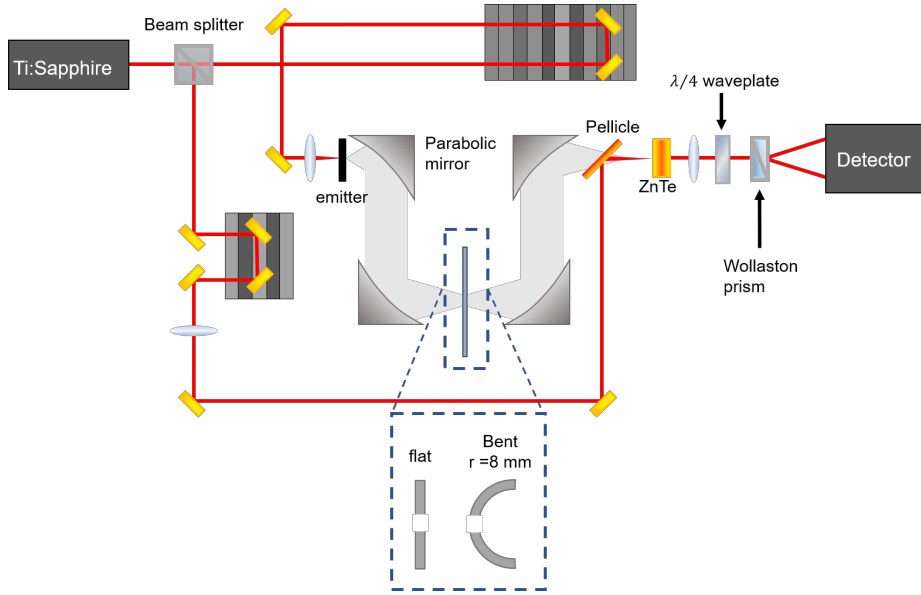


Figure 2.5. A schematic of a transmission-type terahertz time-domain spectroscopy.

2.4. Two-fold resonant behavior

In Figure 2.6, the overall processes are presented in terms of structure (scanning electron microscopy (SEM) image),

simulation (COMSOL multiphysics 5.6), and THz transmittance. First of all, we deliberately investigate structural change from diabolo to bowtie, as shown in Figure 2.6a-d. With increasing bending radius from flat (Figure 2.6a) to $R = 8$ mm (Figure 2.6d), the nanogap becomes wider from 0 to 70, 400, and 650 nm. The corresponding theoretical simulations based on the finite element method are illustrated in Figure 2.6e-h. We mapped the electric-field distributions for each case, where the distinguished electric field is observed between constrictions without (Figure 2.6e) and with (Figure 2.6f-h) the gap. The result indicates the two-fold resonant frequencies of the flat and bent cases. Figure 2.7a is a representative THz transmittance with respect to various bending radius as in Figure 2.6a-d. The pristine diabolo possesses a resonance peak around 0.5 THz (red), and the bent bowtie shows a second-harmonic feature around 1.08 THz (purple). Transmission spectra for other radiuses $R = 20, 15, 13$, and 9 mm are presented between the two spectra (Figure 2.7). We replot the resonant frequencies as following the bending/releasing process (Figure 2.8).

We observe fully covered behavior with the bending and releasing process; namely, the same values are obtained at the boundary. At the boundaries, where the resonance frequency is at 0.5 THz (red) and 1.08 THz (purple), the corresponding electric-field distributions are illustrated, respectively (Figure 2.9). Hrton, M group showed the simulation results of the resonance peaks of the diabolo and the bowtie antenna depending on its length (l) [43] when the p-polarized light interacts with the antenna. They explained that the resonance frequency of the antenna is related to the charge distribution of its geometry. In this manner, the red spots in Figure 2.9 show where the charge accumulates. For instance, when the resonator is flat, the charges accumulate at both ends of the diabolo antenna. When bent, the charges also accumulate at the bowtie gap, which is nearly half-length of the diabolo. As a result, the resonance frequency shifts nearly two-fold as the bending radius reaches 8 mm; on the contrary, it shifts back to the resonant frequency of the pristine diabolo array, operating as a two-fold resonator. Even though the resonance should be two-fold shifted even when the $R = 20$ mm as in the simulation

results (Figure 2.6e-h, left), the diabolo array totally broke into bowtie at $R = 8$ nm in the spectroscopic view (Figure 2.8).

Furthermore, there are threshold-like resonant frequency modulations during flattening (red arrow) and bending (purple arrow). The hysteretic feature may be attributed to elastic limitation during bending and attracting atomic force (flattening) [26,44]. For flattening process, the gap size gradually decreases but negligible change of the resonant frequency is obtained as supported by COMSOL simulation (Figure 2.6e-h and 2.9). Only complete flattening leads to the connection of metal bridge, resulting in the diabolo resonance (red arrow in Figure 2.8). The intermediate resonance frequency observed during bending/releasing process can be explained by weak connection of metal bridge resulting in effective leakage channels such as formation of metal atom chain and location of metal nanoparticles, etc. Depending on effective conductivity inside the gap, the gradual change of resonant frequency can be observed [45-47].

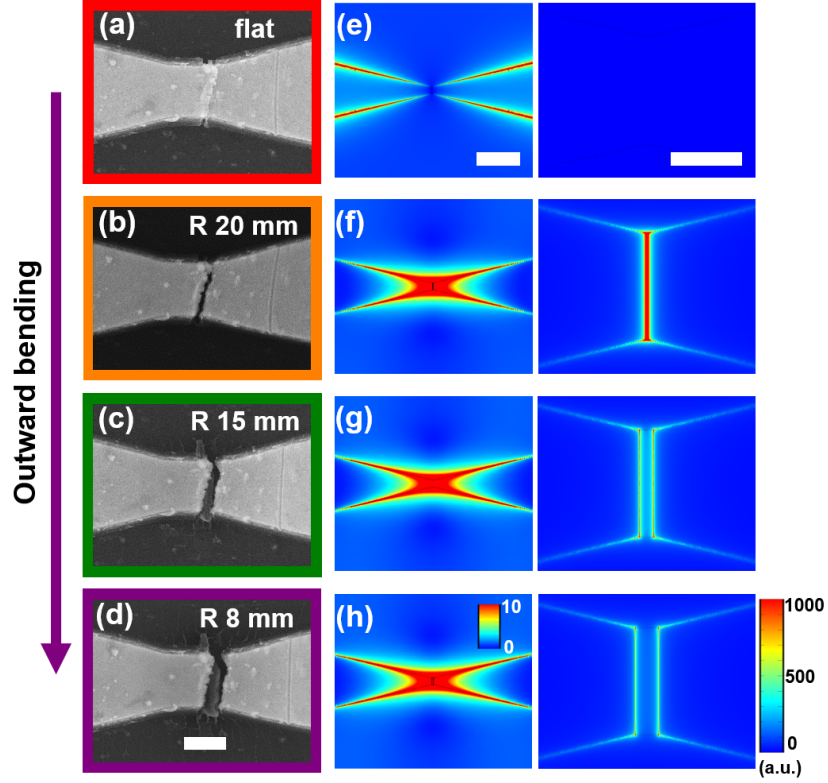


Figure 2.6. Changing the diabolo antenna to a bowtie antenna, increasing the gap depending on its bending radius. (a-d) SEM images for various gaps of 0 nm, 70 nm, 400 nm, and 650 nm with bending radiuses of infinite (flat), 20 nm, 15 nm, and 8 mm, respectively. (e-h) (left) The corresponding electric-field distributions at the gap of the resonator for each bending radius case in (a-d) (simulation results using COMSOL Multiphysics 5.6). (right) Enlarged simulation images at the metallic gap. Scale bars: (a-d) 2 μm ; (e-h, left) 20 μm ; (e-h, right) 2 μm .

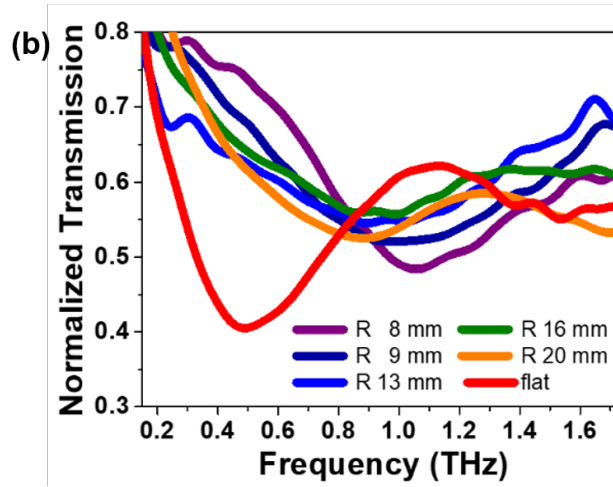
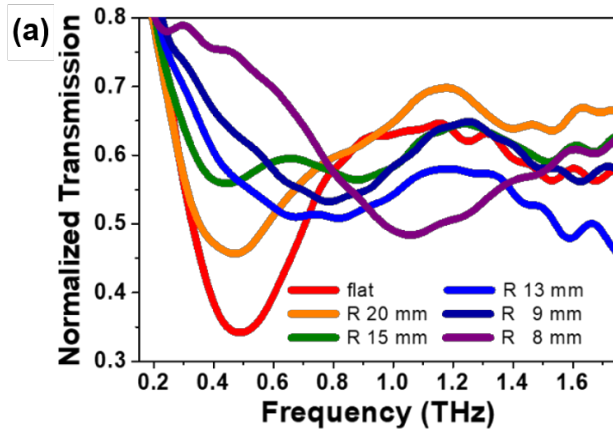


Figure 2.7. Tunable Resonator by gap controlling depending on its bending radius. (a-b) THz transmission spectra for six different bending radiuses. Normalized THz transmission spectra of a two-fold resonator during bending (a) and flattening (b) process.

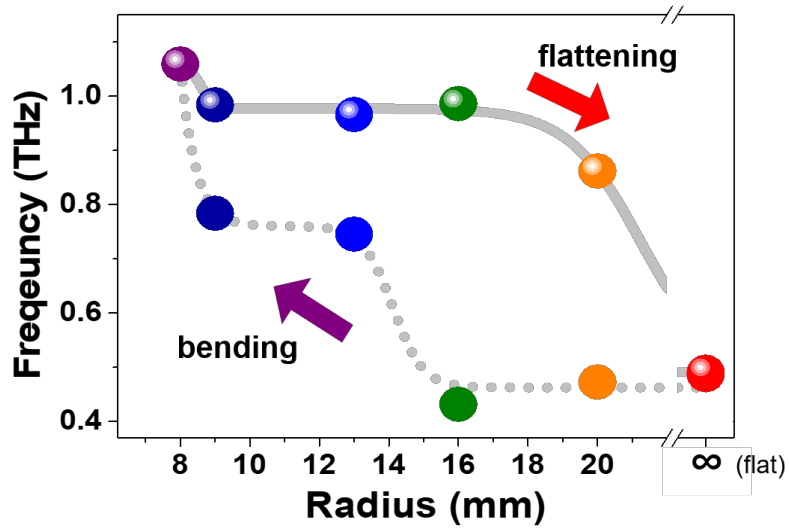


Figure 2.8. Extracted resonant frequencies from (i) as a function of its bending radius. Insets indicate the electric-field distributions for diabolo (top-left), and bowtie antenna (bottom-right).

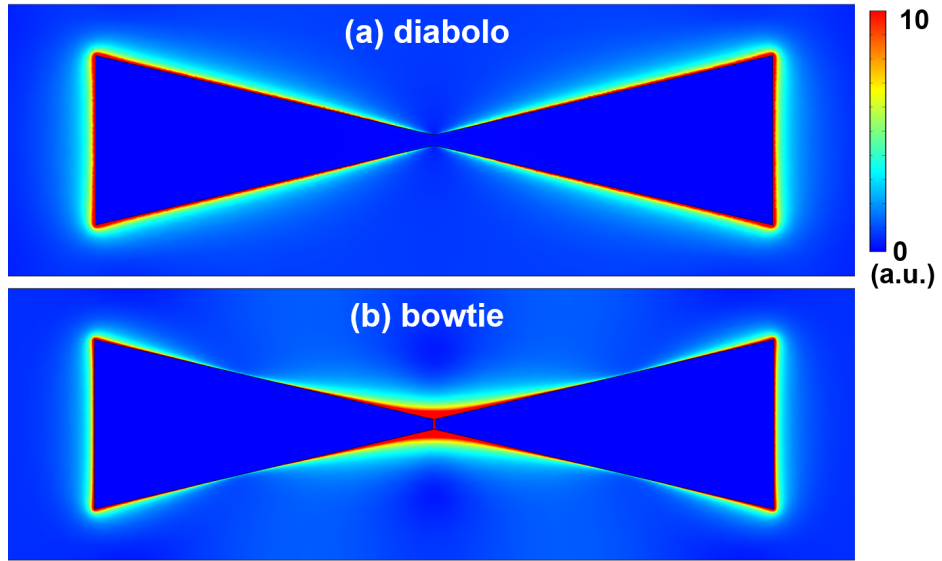


Figure 2.9. The electric-field distributions for the diabolo (a) and bowtie (b) with the gap 500 nm (simulation results using COMSOL Multiphysics 5.6). (right) Diabolo antennas' lengths (l) are $200\text{ }\mu\text{m}$ and the edge-widths (h) are $50\text{ }\mu\text{m}$.

Throughout Figures 2.10-12 show the structural modulation of the THz resonator and the corresponding optical and electrical properties. Figure 2.10a,c and e indicate SEM images for pristine, bent, and released diabolo array, respectively. The pristine diabolo array was designed to be resonant at ~ 0.5 THz, consistent with the resonant dip around 0.5 THz in the THz transmission spectrum (Figure 2.10a). The diabolo was broken near the center after bending (Figure 2.10b), implying that the second-harmonic frequency is expected to be resonant. Indeed, the resonant dip in the transmission spectrum took place around 1.1 THz, well matched with two times of 0.5 Hz. We observed a reversible optical behavior when the bending was released, which follows Figure 2.11 and 2.12. The resonant frequency is precisely coincident with the value of the pristine resonator (Figure 2.10c).

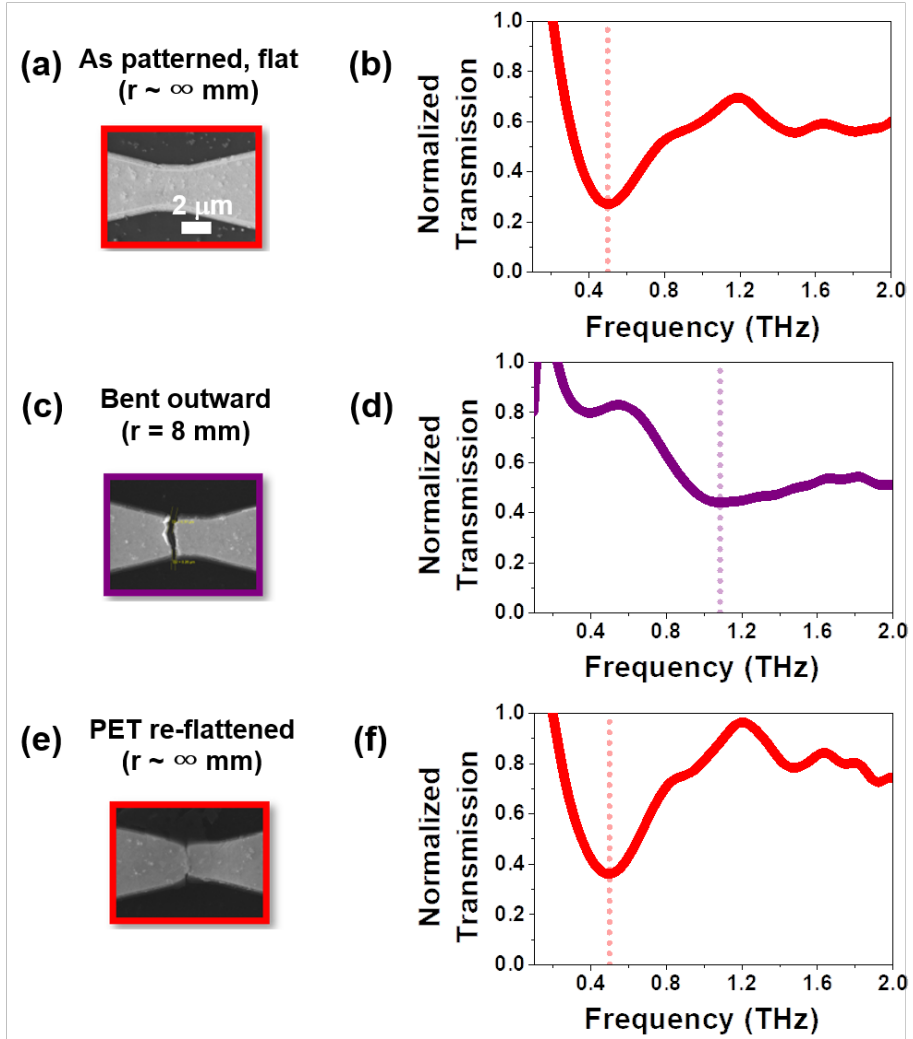


Figure 2.10. Tunable Resonator by gap controlling depending on its bending radius. (a-d) SEM images for various gaps of 0 nm, 70 nm, 400 nm, and 650 nm with bending radiuses of infinite (flat), 20 nm, 15 nm, and 8 mm, respectively. (e-h) (left) The corresponding electric-field distributions at the height of the resonator for each bending radius case in (a-d) (simulation results using COMSOL Multiphysics 5.6). (right) Enlarged simulation images at the metallic gap. (i) THz transmission spectra for six different bending radiuses. (j) Extracted resonant frequencies from (i) as a function of its bending radius. Insets indicate the electric-field distributions for diabolo (top-left), and bowtie antenna (bottom-right). Scale bars: (a-d) 2 μm ; (e-h, left) 20 μm ; (e-h, right) 2 μm .

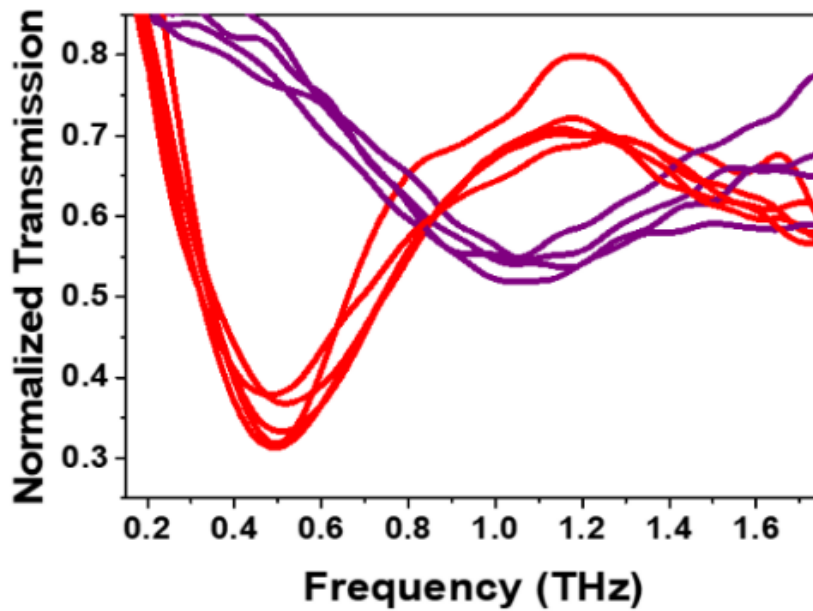


Figure 2.11. Repeatable optical response of a two-fold THz resonator. As repeating the resonator's bending radius as 8 mm (purple lines) and infinite (flat) (red lines), the resonance frequency changes back (0.5 THz) and forth (~1.1 THz).

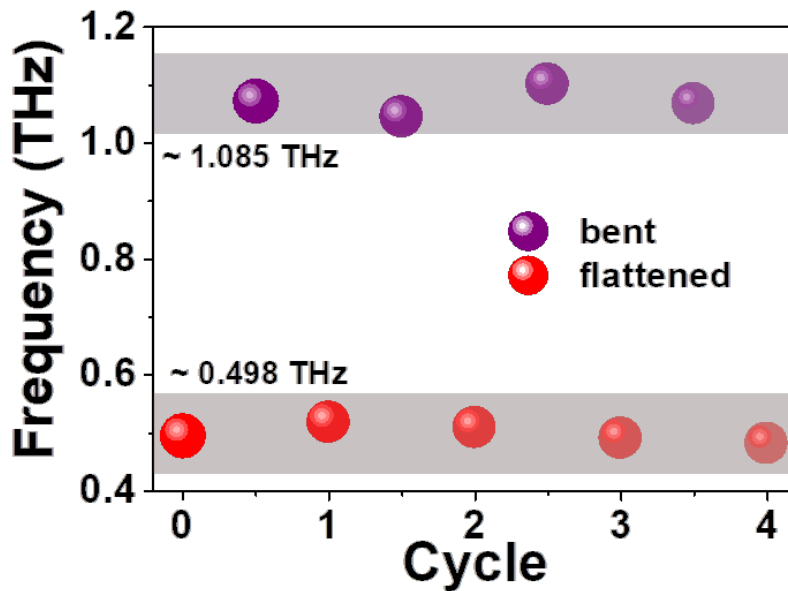


Figure 2.12. Repeatable optical response of a two-fold THz resonator. As repeating the resonator's bending radius as 8 mm and infinite (flat), the resonance frequency changes back (0.5 THz) and forth (~1.1 THz).

The advantages of this flexible two-fold resonator include

its reproducibility and various sensing applications. In this regard, we demonstrate (i) repeatable manipulation of bending/flattening flexible resonator in terms of THz transmittance (Figure 2.10-12) and electrical conductance (Figure 2.13), respectively and (ii) compatibility with molecular biosensing (section 2.5). Both terahertz transmittance (i.e., resonant peak position) and DC conductance exhibit reliable reproducibility, as shown in Figure 2.12 and 2.13, respectively. Note that the conductance $G_0 = 2e^2/h$ (h = Planck constant) is the well-known conductance quantum value referring to a unit of a metallic contact, a single atom of a chain of gold atoms [37,38,48]. In our set-up, the conductance is substantially less than $1 G_0$ when the diabolos is disconnected, and the conductance is large ($\sim 125 G_0$) when they are reconnected. This phenomenon can be repeatably controlled at room temperature.

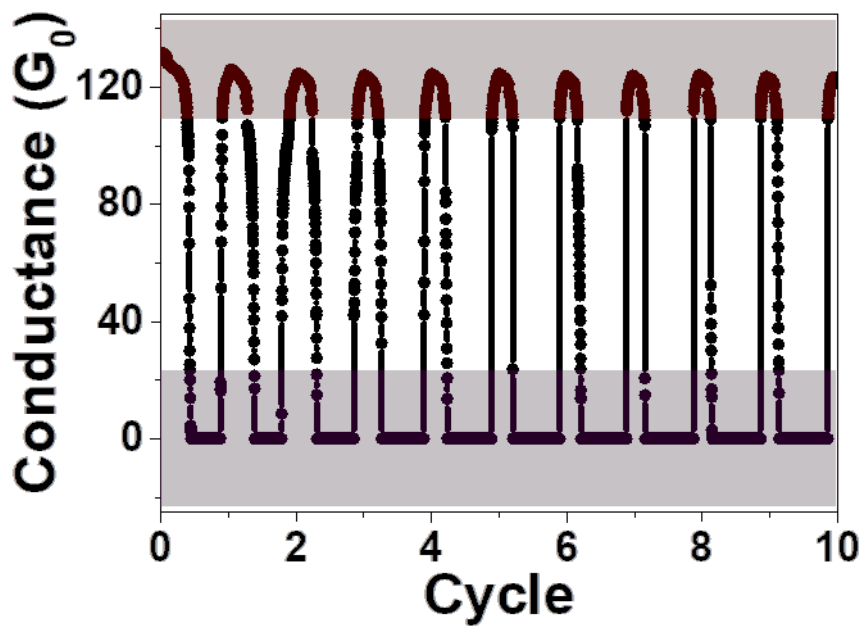


Figure 2.13. Repeatable electrical response of a two-fold THz resonator. The corresponding conductance measurement of figure 2.6.

2.5. Chemical sensing experiment

We confirm that a two-fold resonator can be selectively utilized to detect different molecules. Since intra- and inter-molecular vibration modes lie in the THz regime [49-51], we employ α -lactose and caffeine molecules which possess THz resonant peak around 0.53 THz and 1.25 THz, respectively (See Figure 2.14) [52,53]. We performed four types of experiments: e.g., α -lactose on flatten/bent (Figure 2.15 and 2.17, respectively) and caffeine on flatten/bent (Figure 2.16 and 2.18, respectively). In case of diabolo (bowtie) with resonance frequency of 0.56 THz (1.2 THz), the transmission spectrum more obviously changes for drop-casting of α -lactose (caffeine) molecules compared to that of caffeine (α -lactose) molecules. It is worth to note that the transmission reduction near 1.4 THz for bowtie structures with α -lactose molecules (Figure 2.17) originates from a strong sharp absorption resonance of α -lactose located near 1.4 THz. This implies that sensitive molecular detection via strong light-matter interaction [54-56] becomes possible selectively only

for the condition where the absorption resonance of molecular is well-matched with the resonance of metal structure.

Next, we monitored the transmittance intensity ratio $\Delta T/T_0$ (Figure 2.19a and c) and resonant peak position $\Delta f/f_0$ (Figure 2.19b and d) with respect to the amount of the drop-casting molecules with the help of hotspots induced by antenna array (See Figure 2.6 and 2.9). The flexible resonators sense the target molecule when the bending curvature matches the pristine molecule's resonant frequency. Namely, more apparent changes for α -lactose and caffeine are obtained with flatten and bent resonator, respectively (Figure 2.19a and c): the resonator can sense at least 0.3 mg of lactose (0.2 mg of caffeine) drop-casted with a 6 mm-diameter-sized circular area. Without the resonator hot spot effect, we could observe the absorption peak of 4.8 mg - lactose and 5 mg - caffeine on bare substrate, respectively (Figure 2.14). The lactose (caffeine) molecules show nearly 5% (12%) of the transmittance intensity ratio and 25 GHz (120 GHz) of resonant peak shift, ensuring the sensing property. When the target molecules' absorption resonant and the resonator's

resonant do not match, it is hard to find the sensing property either in transmittance intensity and resonant peak shifts. For instance, as the amount of caffeine on a flattened-resonator increases, the transmission and resonant peak shift changes do not appear consistently (Figure 2.9c and d). For the case of lactose drop-casted on a bent-resonator, the resonant transmission reduction appears at 1.4 THz for 0.6 mg (Figure 2.17b), which is due to the strong second absorption of the lactose molecules (Figure 2.17c). Therefore, the resonant peak position is unlikely to reveal relevant changes with drop-casting amounts (Figure 2.19b and d). It is noteworthy that when a large amount of molecule is dropped, the resonance matching between metal resonator and target molecule is less effective. Even though this experiment is a prototypical demonstration for selective molecular sensing with a two-fold THz resonator, we expect that further improvements in terms of sensitivity and selectivity can be achieved.

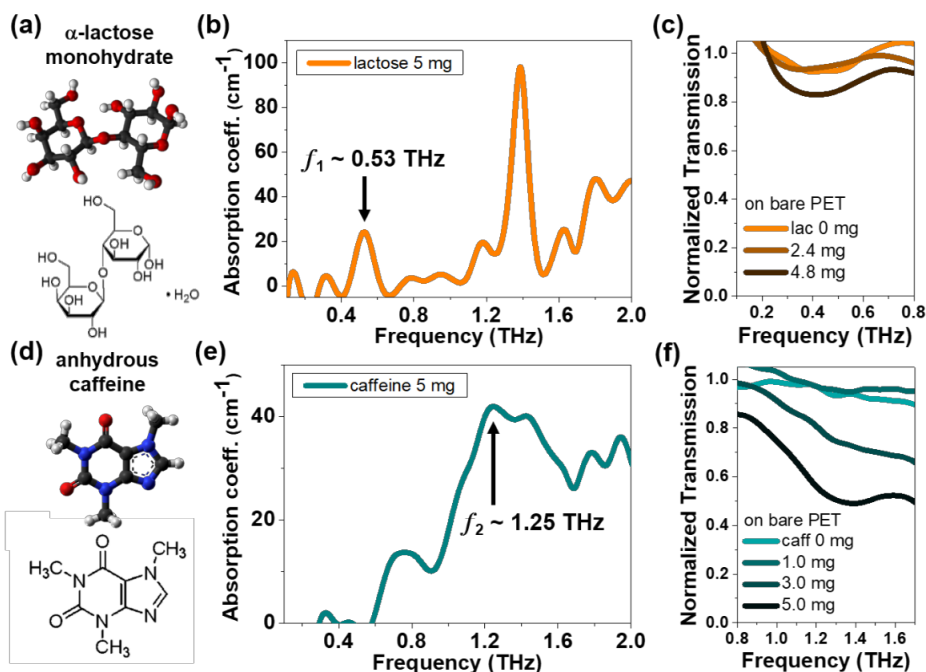


Figure 2.14. Absorption coefficients of lactose monohydrate and anhydrous caffeine powders. (a, d) Molecule structures of lactose (a) and caffeine (d). (b, e) Absorption coefficients for lactose (b) and caffeine (e), showing absorption resonance frequencies around 0.53 THz and 1.25 THz, respectively. (c, f) Normalized transmissions of lactose (c) and caffeine (f) on PET substrate with respect to various amounts of molecules.

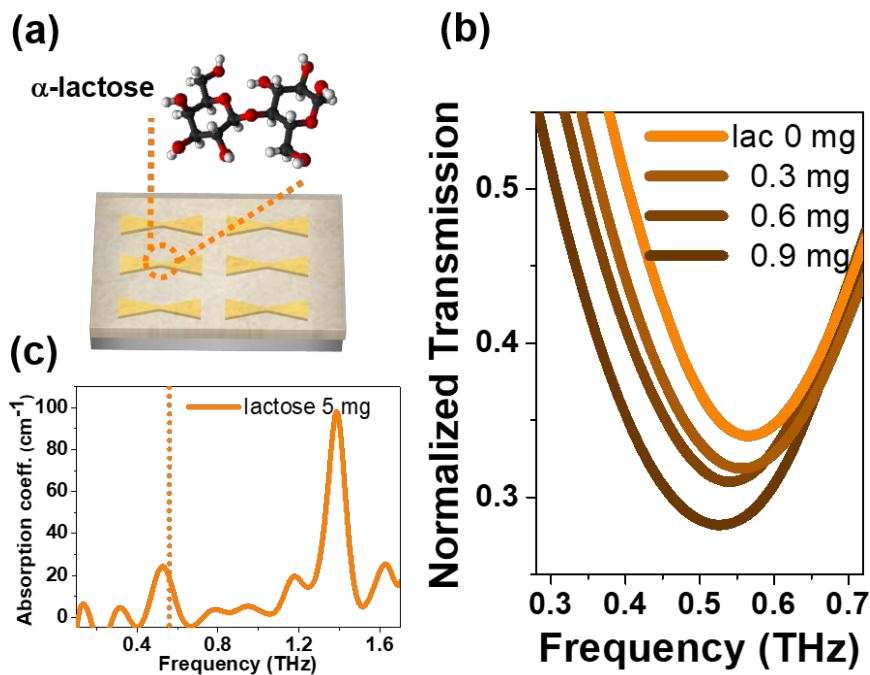


Figure 2.15. Lactose molecular sensing with an array of diabolo (flattened PET substrate). (a) Lactose powders were diluted in methanol and drop-casted on the sample. (b) THz transmission spectra of the case of sensing lactose. (c) Absorption coefficients for lactose showing absorption resonance frequencies around 0.53 THz. The dotted line refers the resonant of the diabolo array.

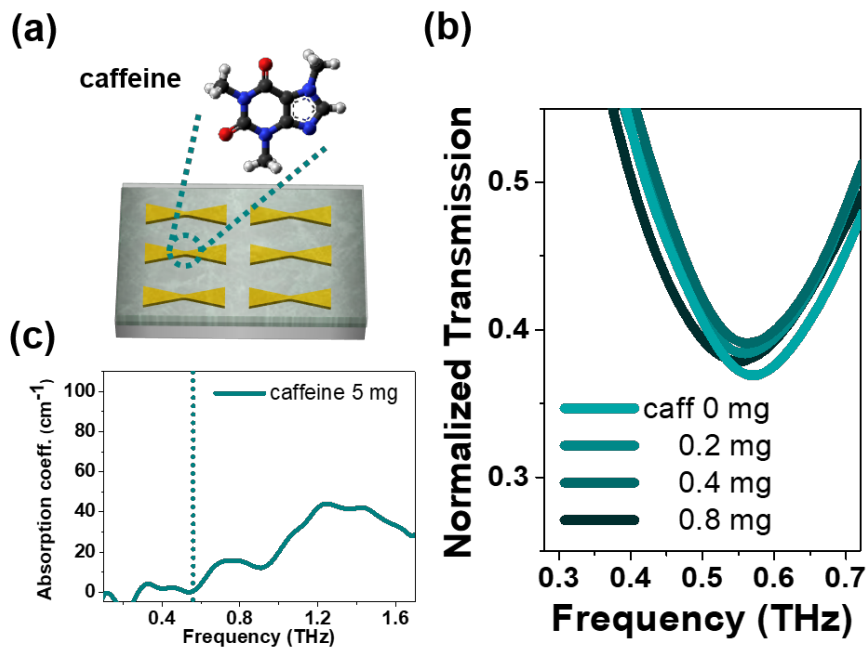


Figure 2.16. Caffeine molecular sensing with an array of diabolo (flattened PET substrate). (a) Caffeine powders were diluted in methanol and drop-casted on the sample. (b) THz transmission spectra of the case of sensing caffeine. (c) Absorption coefficients for caffeine showing absorption resonance frequencies around 1.25 THz. The dotted line refers the resonant of the diabolo array.

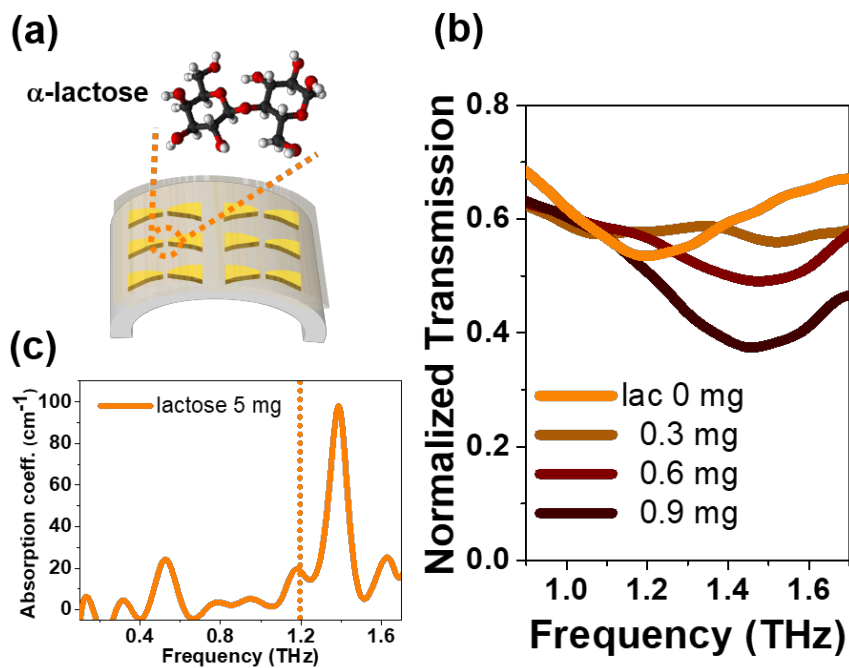


Figure 2.17. Lactose molecular sensing with an array of bowtie (bent PET substrate with a radius of 8 mm). (a) Lactose powders were diluted in methanol and drop-casted on the sample. (b) THz transmission spectra of the case of sensing lactose. (c) Absorption coefficients for lactose showing absorption resonance frequencies around 0.53 THz. The dotted line refers the resonant of the bowtie array.

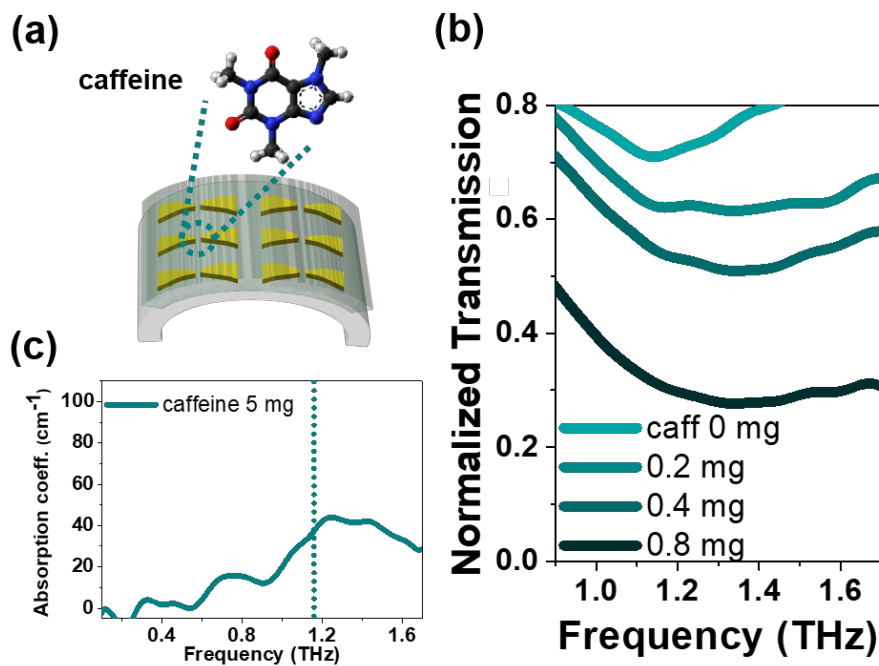


Figure 2.18. Caffeine molecular sensing with an array of diabolo (bent PET substrate with a radius of 8 mm). (a) Caffeine powders were diluted in methanol and drop-casted on the sample. (b) THz transmission spectra of the case of sensing caffeine. (c) Absorption coefficients for caffeine showing absorption resonance frequencies around 1.25 THz. The dotted line refers the resonant of the bowtie array.

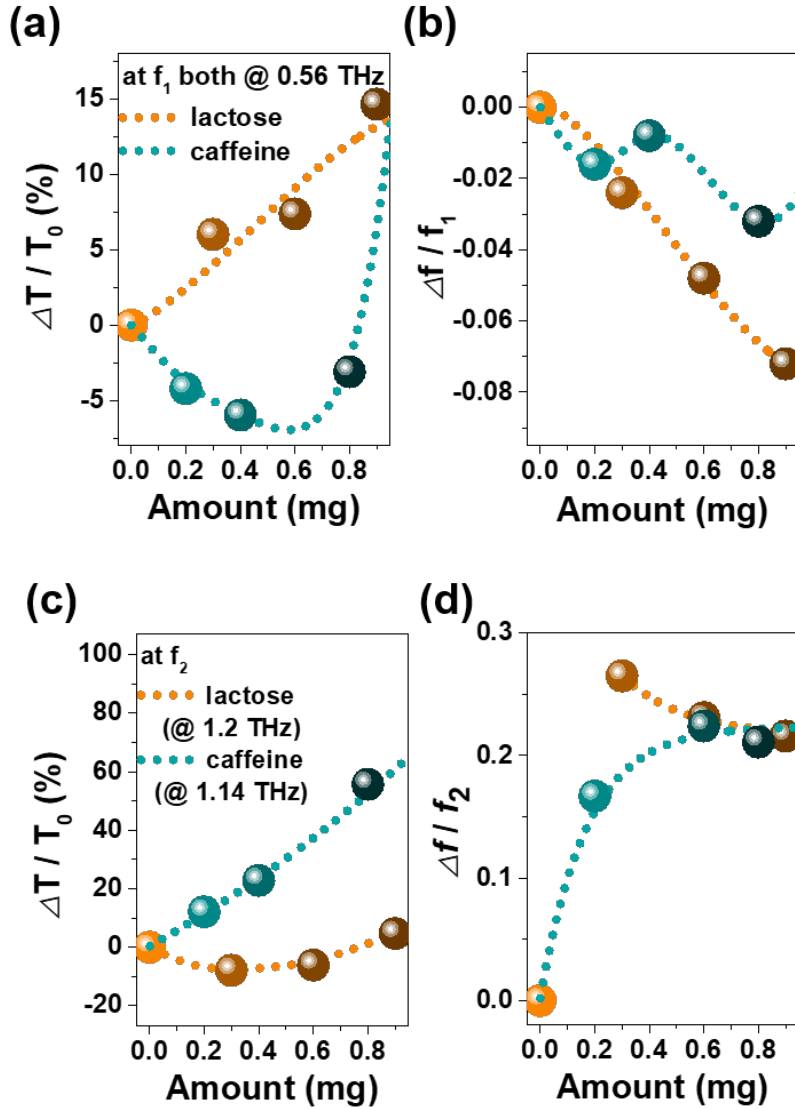


Figure 2.19. Prototypical molecular sensing of tunable resonator by bending substrate. Corresponding transmission change (a) and resonance frequency shift (b) depending on the powder amounts that are extracted from Figure 2.15 and 2.16, respectively. In the same way, the corresponding transmission change (g) and resonance frequency shift (h) compared to that on a bare PET case, are extracted from Figure 2.17 and 2.18, respectively.

Bulk layers of lactose and caffeine are prepared using double-side Kepton tape. We punched a 3 mm-circular hole on

the 5 layered-tape, poured and squeezed 5 mg of lactose (caffeine). The bulk chemical layer was 150 μm thick. Using Beer's law, $\alpha (\text{cm}^{-1}) = -\frac{1}{t} \ln \left(\frac{T}{T_0} \right)$, we obtained the absorption coefficient (α) from THz transmission spectra ($\frac{T}{T_0}$), and the thickness of the bulk layers (t) (Figure 2.8). Lactose and caffeine solutions are prepared in methanol, 5 mg/mL each. We drop-casted every 20 μL drop-by-drop on the array, diabolo and bowtie array separately. After every drop-cast, we dried the sample in air. To obtain a clearer absorption peak, we averaged twenty transmitted THz pulses in THz-TDS and obtained THz transmission spectra.

Chapter 3.

Connectivity – changing resonator by optical tweezing

3.1. Introduction

Optical tweezer researches with plasmonic structures, including such nanopillars [30], nanoholes [31], diabolo nano antenna [32], and chiral structure [33], have been putting efforts to overcome thermal fluctuation of small size of nanoparticles with its enhanced radiation force [34]. Manipulating of small particles with a terahertz (THz) frequency source has inexhaustible potential for spectroscopic researches since most of molecules have their intrinsic vibrational- and rotational- modes at this frequency regime [57-59]. Furthermore, the THz wave is basically non-ionizing and non-destructive electromagnetic wave due to its low photon energy (1 THz corresponds to 4 meV) in the high

repetition rate pulsed system, thus it can be an excellent source for the bio-related application involving cells and biomolecules without any concern about undesirable thermal effect and physical damage [60 -61]. However, a single particle thermal energy is about 26 meV, which is not suitable for optical tweezing. Moreover, a single molecule detection technique requires labelling skills, putting the target molecule in a precise position. An optical tweezer is a representative method for manipulating small particles by optical gradient forces [62-67]. Since the trapping force is proportional to the gradient of incident light intensity, it is possible to put the target particle at the target position. Here, we observed optical tweezing of a 400 nm-sized single gold particle using an incident power of 4 mW focused onto a micrometre spot size and detected it with THz waves using a single bowtie antenna. This study will be a pre-step of a single biomolecule THz detection.

3.2. Preparation of a single bowtie antenna chip and gold nanoparticles

A single bowtie antenna was fabricated by electron-beam lithography on a quartz substrate. We deposited a 3 nm-thick-chromium (Cr) layer in preparation to avoid the charge accumulation phenomena during lithography process. The Electron-beam lithography was performed at an acceleration voltage of 30 keV. We used 950PMMA 7% in anisole (Microchem) as a resist and exposed the electron-beam with $500 \mu\text{C}/\text{cm}^2$. Then, we deposited a 3-nm-thick Cr adhesion layer and a 150-nm-thick gold layer by electron-beam evaporator. The deposition rates were $0.3 \text{ \AA}/\text{s}$ and $0.5 \text{ \AA}/\text{s}$, respectively. The lift-off process was followed using acetone. The sample is ensured by taking the scanning electron microscope (SEM) image of the sample as in Figure 1a and b. The lengths of both wings l of the bowtie antenna were $100 \mu\text{m}$ and the two edge widths of the wings w_1 and w_2 were $25 \mu\text{m}$ and $2 \mu\text{m}$, respectively. The gap-width g in between the wings is 400 nm . The bowtie antenna is tailored to work as a

resonator with a nanoscale field confinement in the terahertz frequency regime.

The 400-nm-sized gold nanoparticles are supplied in 0.1 mg/mL sodium citrate with stabilizer, water (Thermo scientific). We diluted 0.1% of the nanoparticle's suspension in the deionized water. We vortexed the solution for 30 minutes to avoid the aggregation of the gold nanoparticles. As in the Figure 1c, the size of the gold particles varies from 380 nm to 420 nm.

We used a 10- μ m-thick double-sided tape (Thin PET-based Double-sided Tape No.5601, Nitto Denco Corporation) as a spacer in between the substrate of the antenna sample chip and the 150- μ m-thick cover-slip (Marienfeld). The tape was 15-mm-wide and 15-mm-long, and we punched an 8-mm-wide 8-mm-long square hole in the middle. We dropped 0.5 μ L of the gold particle solution using a micro-pipette (Pipetman P2, Gilson) and enclosed it with the cover-slip. The sizes of the sample substrate and the cover-slip were 15 mm by 15 mm and 18 mm by 18 mm, respectively, that are large enough to enclose the solution. The solution inside the sample chip last

for two-weeks ensuring no leakage during the experiment.

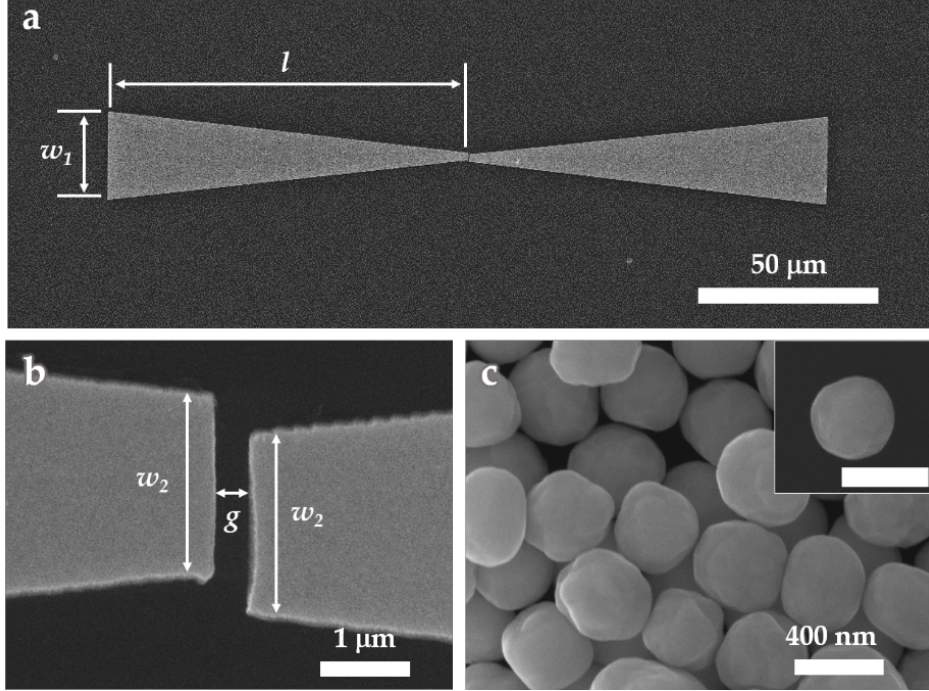


Figure 3.1. Sample preparation. (a) The scanning electron microscope (SEM) image of a single bowtie antenna on a quartz substrate fabricated by electron-beam lithography. The length l is $100\text{ }\mu\text{m}$ and widths w_1 and w_2 are $25\text{ }\mu\text{m}$ and $2\text{ }\mu\text{m}$, respectively; (b) The enlarged version of the figure (a). The gap size g is 400 nm ; (c) SEM image of 400-nm -sized gold nanoparticles. Inset: a single gold nanoparticle. Scale bar: 400 nm .

3.3. Top-down optical tweezing THz

probe system

The experimental concept is illustrated in Figure 3.2 (a). The bowtie antenna is encapsulated as a chip covered with cover glass, and inside it, the gold nanoparticle solution is contained. The optical tweezing beam from the top of the antenna locates the particle at the center of the bowtie antenna, and at the same time the incident terahertz pulse illuminates from the bottom of the sample chip.

The collimated wavelength of 788 nm laser beam (Part number 1069416, Cube laser 40 mW, Coherent) and the oil immersion lens with NA 1.45 (PlanApo 60x Olympus) are used to tweeze a single gold nanoparticle. The working distance of the lens was 0.17 mm, which was able to focus on the surface of the substrate. It is noteworthy that the total thickness of the spacer and the covers-slip is 0.16 mm which is less than the working distance of the optical lens. The tungsten halogen lamp illuminated on the sample to visualize the optical tweezing experiment at real-time through the charge-coupled device (CCD) camera (Thorlabs). The pixel resolution as 1280

x 1024, with the frame rate of 38 frame per seconds (fps).

This terahertz reflection setup obtains the reflection spectra from 0.15 THz to 2 THz with the averaged signal-to-ratio of 67 dB (Figure 3.2b). The setup was based on an electro-optic sampling version of terahertz-time domain spectroscopy (Figure 3.2c). A mode -locked Ti:sapphire femtosecond laser of 800-nm-centered wavelength (80 MHz repetition rate, 100 fs pulse width) was used to run the system. The collimated laser beam splits into two by the beam splitter (BS), named pump-beam (transmitted 98%) and probe-beam (reflected 2%). The pump-beam illuminated at the low-temperature GaAs photoconductive antenna, called emitter, and generated the terahertz pulses. These pulses were guided by the 1st and the 2nd off-axis parabolic mirrors and illuminated from the bottom of the sample's substrate. The reflected signals from the sample were gathered by the 3rd parabolic mirror. The 1.5-mm-thick silicon-beam splitter (Si-BS) is used to guide the reflected pulses to ZnTe crystal. The probe-beam was guided by the mirrors and the pellicle that transmits 70% of the 800-nm-wavelength-beam (Thorlabs).

The manual delay stage in the probe beam line was used for matching the length of the pump beam line. The probe beam is also focused on the ZnTe crystal. The electro-optic crystal (ZnTe) detected these terahertz signals in time domain. The polarization of the incident laser beam changes proportionally to the incoming terahertz field compared to the probe beam in this crystal due to the Pockels effect [68]. The Wollaston prism splits the linear polarization components in horizontal direction and in vertical direction, serving the input to the photo-detector (Nirvana Balanced Receiver, Newport). The terahertz beam spot size on the sample is measured as 0.96 mm. The sample is centered by monitoring it with the optical microscope and by moving the sample with the 3-axis stage.

The terahertz setup is purged with nitrogen gas, stabilizing the humidity less than 7% to minimize the water absorption effect. Since the skin depth at 1 THz is 80 nm, a 150-nm-thick gold film is regarded as a perfect electric conductor [69]. In the time domain, we extract the reference signal that indicates the reflectance at the interface in between the gold film and the substrate. Next, we take the sample and the substrate

reflection signals in time domain, respectively. The extracted sample film effect is obtained by eliminating the substrate signals from the sample signals. By Fourier-transforming these two signals, the reflected normalized amplitude is defined as $E_{\text{sam}}(w)/E_{\text{ref}}(w)$, where E_{sam} and E_{ref} are reflected electric fields from the sample and the gold film, respectively.

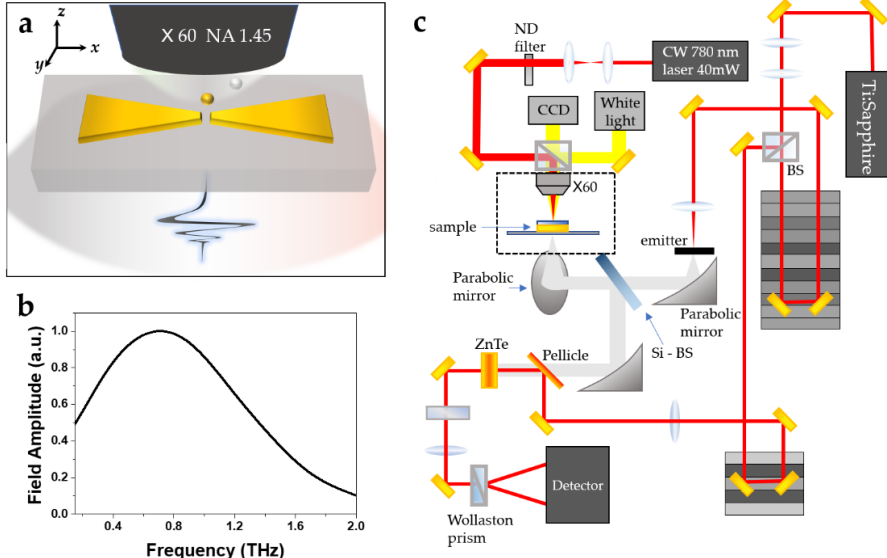


Figure 3.2. The experimental setup. (a) A schematic of the experimental concept. While holding the gold nanoparticle on the bowtie antenna with optical tweezing beam from the top of the antenna, the reflected terahertz beam observes whether the particle locates in between the gap by illuminating the terahertz beam from the bottom of the substrate.; (b) Field amplitude spectrum of the reference pulse. The 150-nm-thick gold film on the quartz substrate is used as the reference sample.; (c) A scheme of the experimental setup combining optical tweezing and reflection type terahertz-probe setup. The terahertz reflection setup is based on terahertz-time domain spectroscopy.

3.4. Stabilized optical tweezing conditions

An experimental way to show that a particle is trapped in

$$\text{diffraction limit } d \sim \frac{\lambda}{2 \cdot NA}, \text{ where } \lambda = 788 \text{ nm, and } NA = 1.45, \quad (3.1)$$

the tweezing beam is to take a video and analyze the particle's movement [64, 70]. If the particle's movement is much smaller than the diffraction limit of the tweezing beam wavelength, the particle is stably trapped in the laser beam [71-73]. The motion-captured CCD images from the particle-trapping video are shown in Figures 3.3a and b. A 400 nm-sized particle is in the center of the tweezing beam when trapped (Figure 3.3a), and no particle is in the beam when released (Figure 3.3b) where the tweezing beam power is 6 mW. The motion-captured video comprises 189 by 183 pixels, and the length per pixel is 20 nm. The spatial resolution of the pixel is about 5% of the particle size. And since the wavelength of the tweezing beam is 788 nm and the NA value of the objective lens is

1.45, the diffraction limit is ~ 272 nm as the followed equation,

Based on the video, after plotting the motion of particles in the x-y space as shown in Figure 3.3c, the distance from the center of the trapping beam in the x-direction (horizontal direction) and y-direction (vertical direction) are plotted in the

histogram distribution as in Figures 3.3d and e. The histogram distribution can be interpreted as a probability distribution where the particle exists from the center, which can be fitted with a Gaussian normal distribution (red line in Figure 3d, blue line in Figure 3.3e) [10, 64, 71-73]. The particle's motion Δx and Δy correspond to the Gaussian distribution standard deviation [73]. The particle motions Δx is about 29.2 nm, and Δy is about 25.7 nm in Figures 3.3d and e. The motions in the x-direction and the y-direction are much smaller than the diffraction limit ($d \sim 272$ nm) of the tweezing beam wavelength, so the particle is stably trapped in the tweezing beam.

There is another condition for stably trapping particles, as specified in A. Ashkin et al. Optics Lett. in 1986, trapping potential amplitude $U(x \text{ or } y)$ should satisfy the condition of the following equation,

$$\exp(U(x \text{ or } y)/k_B T) \ll 1, \quad (3.2)$$

where k_B denotes Boltzmann constant, T denotes temperature (room temperature ~ 300 K), and $k_B T$ denotes the kinetic energy of Brownian motion at room temperature, corresponding 25.7 meV , $4.11 \text{ pN} \cdot \text{nm}$ (4.11×10^{-21} J) [72].

As mentioned in the Neumann et al. Rev. Sci. Instru. in 2004, if the particle motion can be represented by a Gaussian distribution, the trapping potential measurement can be obtained from the Boltzmann probability density function,

$$p(x \text{ or } y) = \exp\left(\frac{-U(x \text{ or } y)}{k_B T}\right) / Z, \quad (3.3)$$

where Z is a partition function normalizing the probability density function [10, 73].

Considering the Gaussian distribution in Figures 3d and e as the Boltzmann probability density function, the trapping potential can be obtained as following,

$$U(x \text{ or } y) = -\ln Z - \ln(p(x \text{ or } y)), \quad (3.4)$$

By substituting the probability $p(x \text{ or } y)$ and the partition function Z from the histogram and the Gaussian fitting in Figures 3.3d and e into the equation (4), we can plot the trapping potential U according to the distance in x- and y-direction (Figure 3.3f). The potential values obtained from the histogram are shown as red and blue lines, and the potential values obtained from the Gaussian fitting are shown as red dotted lines and blue dotted lines. The amplitude of $U(x)$ is

$4.07 k_B T$, and $U(y)$ is $4.10 k_B T$, so the trapping potentials satisfy the conditional equation (2). Therefore, the particles are stably trapped according to the second trapping condition (equation (2)).

The value of trapping stiffness k is also mentioned in optical tweezing studies for checking whether the particle is stably trapped [10, 71-73]. This is because a trapped particle in the tweezing beam moves around the beam center, so the trapping force is $F = k \cdot \Delta x$, regarding as having a spring between the particle and the center of the beam. The trapping potential value can be expressed as,

$$U(x \text{ or } y) = \frac{1}{2} k (\Delta x \text{ or } \Delta y)^2. \quad (3.5)$$

The trapping stiffnesses k_x and k_y can be obtained from the potential in Figure 3f and Δx and Δy in Figures 3 d and e, respectively. The experimental values $k_x \sim 6.54 \text{ pN/nm} \cdot W$ and $k_y \sim 8.50 \text{ pN/nm} \cdot W$. The references showed a stable particle trapping result with $k \sim 0.51 \text{ pN/nm} \cdot W$ when trapping a 250 nm-sized-gold particle and $k \sim 0.69 \text{ pN/nm} \cdot W$ when trapping a 300 nm-sized- polystyrene bead [64, 74]. Therefore, regarding the

trapping stiffness, we determine that the particle is stably trapped in the tweezing beam.

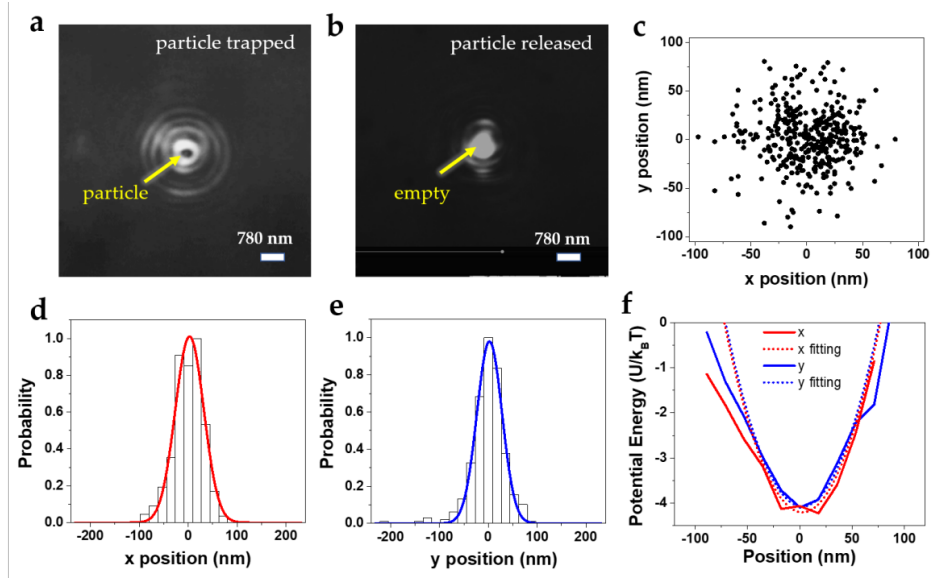


Figure 3.3. Tracking the movements of an optical-trapped single gold nanoparticle. (a) A charged-couple device (CCD) image of a particle trapped inside the focal tweezing beam; (b) A CCD image of a particle released version, there is no particle inside the focal beam spot compared to (a); (c) The measured position distribution of a optical-tweezed particle; (d) The histogram of the probability density plotted as a function of the distance in x-direction from the origin of (c). The red line denotes the Gaussian distribution fitting curve; (e) The histogram of the probability density plotted as a function of the distance in y-direction from the origin of (c). The blue line denotes the Gaussian distribution fitting curve; (f) The trapping potential energy along the x (red) and y (blue) axes extracted from (d) and (e). The dotted lines are extracted from the fitting curves in (d) (red dotted line) and (e) (blue dotted line).

3.5. A single gold nanoparticle detection in THz reflection spectrum

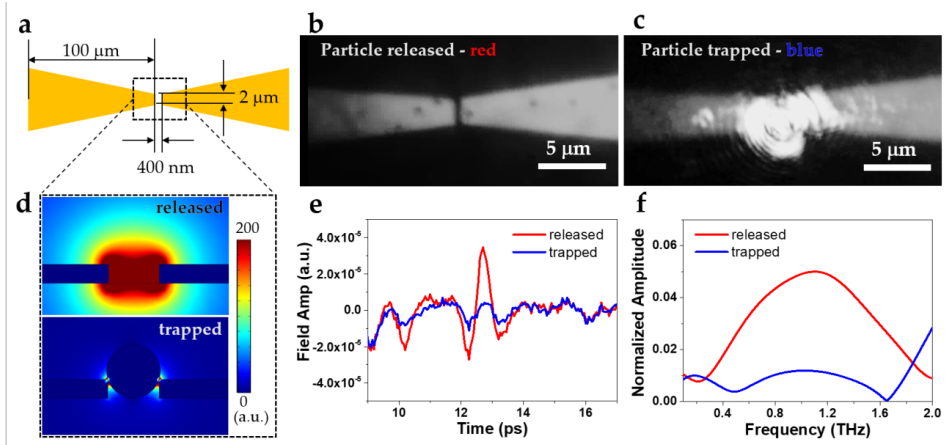


Figure 3.4. Detecting a single gold nanoparticle in THz spectrum. (a) A schematic of the bowtie antenna used for the experiment and theoretical analyzation. The length of the wings ($l = 200 \mu\text{m}$), the edge width ($w_2 = 2 \mu\text{m}$), and the gap width ($g = 400 \text{ nm}$) are mentioned in (a).; (b) the CCD image of the center of the bowtie antenna, while the THz beam is illuminated and the optical tweezing beam is blocked.; (c) the CCD image of the center of the bowtie antenna, while both THz beam and the optical tweezing beam are illuminated on the sample.; (d) the cross-sectional view of the electric field distributions illustrated by COMSOL 5.6 for the case of without (top) and with the particle in between the gap (bottom) of the bowtie antenna. The particle size is 420 nm . The distance from the substrate is 4 nm .; (e) Time traces of the reflected THz electric field at the interface substrate-sample layer for the particle released ((b), red line) and trapped in the bowtie antenna gap ((c), blue line). The reflection from the bare substrate data is subtracted from both data; (f) The normalized reflected amplitudes of the case of (b) (red line) and (c) (blue line) in frequency domain.

We have checked the sample, THz setup, and optical tweezing stabilization. Here, we show the experimental results detecting a 400 nm -sized particle in the THz reflection spectrum by optically tweezing the particles on a single antenna. When we look through the CCD image, it is unknown

whether tweezing particles are in the gap due to tweezing beam light reflected by the metallic antenna. However, we can ensure that the particle is in the gap with the terahertz reflection spectrum in real-time. In the terahertz reflection time trace, the reflection data of the bare substrate part is removed from 'the single bowtie data', and the data of the red line is obtained. Similarly, we remove the reflection data of the bare substrate part from 'the bowtie with particle trapping data' and obtain the data of the blue line.

We Fourier transformed these data (red and blue time traces) to obtain spectral reflection data as f . The comsol simulation plots show cross-sectional electric distributions with and without particles in the gap.

When particles are trapped, the enhanced field volume in the near-field is reduced, indicating that the reflectance observed in the far-field is relatively small. This experimentally confirmed gold particle tweezing on a single bowtie antenna.

Chapter 4.

Conclusion

Based on the shape of the bowtie antenna, the connectivity of the metallic nanogap of the antenna was manipulated by mechanical bending and optical tweezing, and the optical response in the THz spectrum was observed. We proposed a novel type of a chip-scaled active resonator by mechanical bending of a THz metal antenna. Breaking-induced structure changed from diabolo to bowtie renders the resonant frequency reversible and two-fold, confirmed by theoretical simulation and the THz transmission spectra. Using the tunable two-fold feature, we further demonstrated molecular sensing, where resonant frequency corresponds to a two-fold metal antenna. Consequently, detecting a minute amount of molecule was achieved with resonant-frequency-matched bending. This mechanical manipulation is tunable between two resonances and can be utilized for flexible active devices.

Furthermore, a gold nanoparticle was manipulated by optical tweezing to put it inside the particle-sized gap of the single bowtie antenna, and at the same time, the reflectance amplitude was reduced in the THz spectrum.

Chapter 5.

Appendix

5.1. Sub 10 nm Nanogap fabrication

Each method is basically used to form sub-10 nm wide gaps between the metals carried out by photolithography, metal deposition, ALD and the exfoliation processes (Figure 6.1). The first step is to pattern the first metal frame by photolithography, making a rectangular hole array in a metallic thin film. In photolithography process, we designed the Cr photomask to make the in-plane dimensions of method 1 to 5 as the patterns of $10\text{ }\mu\text{m}$ (l_x) \times $10\text{ }\mu\text{m}$ (l_y), $10 \times 40\text{ }\mu\text{m}$, $50 \times 50\text{ }\mu\text{m}$, and $3\text{ mm} \times 5\text{ mm}$. This is intended to show that the samples can be made regardless of the in-plane dimensions. The second step is to coat a few nanometer thick insulator (alumina) layer over the whole structure by ALD. The third step is to deposit second metallic films which are for filling

the hole of the first metallic frame and forming metal-insulator-metal (MIM) nanogap structures. At last, we exfoliate the unnecessary metallic film by using a tape or a chemical etchant to expose nanogaps for optical purposes.

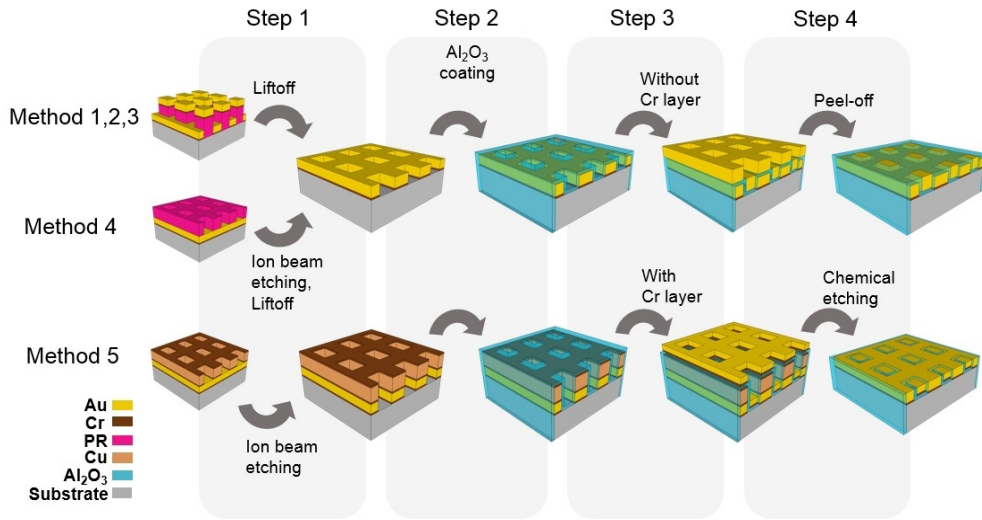


Figure 6.1 Schematic illustrations of stepwise procedures of the five methods consisting of four steps; first metallic frame formation, ALD process, second metallic film deposition, and the exfoliation process. At step 1, the first metallic frame is formed by photolithography, metal deposition, and liftoff in methods 1, 2, and 3. Photoresist pattern (pink) is used as a shadow mask for ion beam etching and after the liftoff the first metallic frame is formed in Method 4, while a metallic pattern is used for a shadow mask in method 5.

Bibliography

1. Novotny, L., and Van Hulst, N., Antennas for light, Nat. Photon. 5 (2), 83-90 (2011).
2. Giannini, V., Fernández-Domínguez, A. I., Heck, S. C., and Maier, S. A., Plasmonic Nanoantennas: Fundamentals and Their Use in Controlling the Radiative Properties of Nanoemitters, Chem. Rev. 111 (6), 3888-3912 (2011).
3. Fu, Q., Zhan, Z., Dou, J., Zheng, X., Xu, R., Wu, M., and Lei, Y., Highly Reproducible and Sensitive SERS Substrates with Ag Inter-Nanoparticle Gaps of 5 nm Fabricated by Ultrathin Aluminum Mask Technique, ACS Appl. Mater. Interfaces 7 (24), 13322-13328 (2015)
4. Yokota, Y., Ueno, K., and Misawa, H., Essential nanogap effects on surface-enhanced Raman scattering signals from closely spaced gold nanoparticles. Chem. Commun. 47 (12), 3505-3507 (2011).
5. Flauraud, V., van Zanten, T. S., Mivelle, M., Manzo, C., Garcia Parajo, M. F., and Brugger, J., Large-Scale Arrays of

- Bowtie Nanoaperture Antennas for Nanoscale Dynamics in Living Cell Membranes, *Nano Lett.* 15 (6), 4176-4182 (2015).
6. Aksu, S., Cetin, A. E., Adato, R., and Altug, H., Plasmonically Enhanced Vibrational Biospectroscopy Using Low-Cost Infrared Antenna Arrays by Nanostencil Lithography, *Adv. Opt. Mater.* 1 (11), 798-803 (2013).
 7. Jeong, Y. G., Paul, M. J., Kim, S. H., Yee, K. J., Kim, D. S., and Lee, Y. S., Large enhancement of nonlinear terahertz absorption in intrinsic GaAs by plasmonic nano antennas, *Appl. Phys. Lett.* 103 (17), 171109 (2013).
 8. Bahk, Y. M., Kang, B. J., Kim, Y. S., Kim, J. Y., Kim, W. T., Kim, T. Y., Kang, T., Rhie, J., Han, S. H., Park. C. H. Rotermund, F., and Kim, D. S., Electromagnetic saturation of angstrom-sized quantum barriers at terahertz frequencies., *Phys. Rev. Lett.* 115 (12), 125501 (2015).
 9. Engheta, N., Circuits with Light at Nanoscales: Optical Nanocircuits Inspired by Metamaterials, *Science* 317 (5845), 1698-1702 (2007).

10. Juan, M. L., Righini, M., and Quidant, R., Plasmon nano-optical tweezers, *Nat. Photon.* 5 (6), 349-356 (2011).
11. Maragò, O. M., Jones, P. H., Gucciardi, P. G., Volpe, G., and Ferrari, A. C., Optical trapping and manipulation of nanostructures, *Nat. Nanotech.* 8 (11), 807-819 (2013).
12. Jeong, J., Rhie, J., Jeon, W., Hwang, C. S., and Kim, D. S., High-throughput fabrication of infinitely long 10 nm slit arrays for terahertz applications, *J. Infrared Millimeter Terahertz Waves* 36 (3), 262-268 (2014).
13. Lee, K., Jeong, J., Bahk, Y. M., Rhie, J., Baek, I. K., Lee, B. J., Kang, Y.H., Hong, S., Park, G. S., and Kim, D. S. Microwave Funneling through Sub-10 nm Nanogaps, *ACS Photonics* 3 (4), 537-542 (2016).
14. Kang, T., Rhie, J., Park, J., Bahk, Y. M., Ahn, J. S., Jeon, H., and Kim, D. S., Resonance tuning of electric field enhancement of nanogaps, *Appl. Phys. Express* 8 (9), 092003 (2015).
15. Genet, C., and Ebbesen, T. W., Light in tiny holes, *Nature* 445 (7123), 39-46 (2007).

16. Seo, M. A., Park, H. R., Koo, S. M., Park, D. J., Kang, J. H., Suwal, O. K., Choi, S. S., Planken P. C. M., Park, G. S. , and Kim, D. S., Terahertz field enhancement by a metallic nano slit operating beyond the skin-depth limit, *Nat. Photon.* 3 (3), 152-156 (2009).
17. Chen, X. S., Park, H. R., Pelton, M., Piao, X. J., Lindquist, N. C., Im, H., Kim, Y. J., Ahn, J. S., Ahn, K. J., Park, N., Kim, D. S., and Oh, S. H., Atomic Layer Lithography of Wafer-scale Nanogap Arrays for Extreme Confinement of Electromagnetic Waves. *Nat. Commun.*, 4(1), 1-7 (2013).
18. Huang, Y.-W., Lee, H. W. H., Sokhoyan, R., Pala, R. A., Thyagarajan, K., Han, S., Tsai, D. P., Atwater, H. A., Gate-tunable Conducting Oxide Metasurfaces. *Nano Lett.*, 16 (9), 5319-5325 (2016).
19. Kern, J., Kullock, R., Prangsma, J., Emmerling, M., Kamp, M., Hecht, B., Electrically driven optical antennas. *Nat. Photonics* 9 (9), 582-586 (2015).
20. Zhu, W., Liu, A., Bourouina, T., Tsai, D. P., Teng, J., Zhang, X., Lo, G., Kwong, D., Zheludev, N., Microelectromechanical

- Maltese-cross Metamaterial with Tunable Terahertz Anisotropy. *Nat. Commun.*, 3 (1), 1-6 (2012).
21. Ju, L., Geng, B. S., Horng, J., Girit, C., Martin, M., Hao, Z., Bechtel, H. A., Liang, X. G., Zettl, A., Shen, Y. R., Wang, F., Graphene Plasmonics for Tunable Terahertz Metamaterials. *Nat. Nanotechnol.*, 6 (10), 630-634 (2011).
22. Degl'Innocenti, R., Jessop, D. S., Shah, Y. D., Sibik, J., Zeitler, J. A., Kidambi, P. R., Hofmann, S., Beere, H. E., Ritchie, D. A., Low-Bias Terahertz Amplitude Modulator Based on Split-Ring Resonators and Graphene. *ACS Nano*, 8 (3), 2548-2554 (2014).
23. Chen, H. T., O' Hara, J. F., Azad, A. K., Taylor, A. J., Averitt, R. D., Shrekenhamer, D. B., Padilla, W. J., Experimental Demonstration of Frequency-agile Terahertz Metamaterials. *Nat. Photonics*, 2 (5), 295-298 (2008).
24. Jeong, Y. G., Han, S., Rhie, J., Kyoung, J. S., Choi, J. W., Park, N., Hong, S., Kim, B. J., Kim, H. T., Kim, D. S., A Vanadium Dioxide Metamaterial Disengaged from Insulator-to-Metal Transition. *Nano Lett.*, 15 (10), 6318-6323 (2015).

- 25.Pryce, I. M., Aydin, K., Kelaita, Y. A., Briggs, R. M., Atwater, H. A., Highly Strained Compliant Optical Metamaterials with Large Frequency Tunability., *Nano Lett.*, 10 (10), 4222-4227 (2010).
- 26.Kim, D., Yun, H. S., Das, B., Rhie, J., Vasa, P., Kim, Y.-I., Choa, S.-H., Park, N., Lee, D., Bahk, Y.-M., Kim, D. S., Topology-Changing Broadband Metamaterials Enabled by Closable Nanotrenches. *Nano Lett.*, 21 (10), 4202-4208 (2021).
- 27.Das, B., Yun, H. S., Park, N., Jeong, J., Kim, D. S., A Transformative Metasurface Based on Zerogap Embedded Template. *Adv. Opt. Mater.*, 2002164, (2021).
- 28.Song, L., Myers, A. C., Adams, J. J., Zhu, Y., Stretchable and reversibly deformable radio frequency antennas based on silver nanowires. *ACS Appl. Mater. Interfaces*, 6 (6), 4248-4253, (2014).
- 29.Li, J., Shah, C. M., Withayachumnankul, W., Ung, B. S.-Y., Mitchell, A., Sriram, S., Bhaskaran, M., Chang, S., Abbott, D., Mechanically tunable terahertz metamaterials. *Appl. Phys. Lett.*, 102 (12), 121101 (2013).

30. Wang, K., Schonbrun, E., Steinvurzel, P., Crozier, K. B.,
Trapping and rotating nanoparticles using a plasmonic
nano-tweezer with an integrated heat sink. *Nature Commun.*
2, 469 (2011).
31. Juan, M. L., Gordon, R., Pang, Y., Eftekhari, F., Quidant, R.,
Self-induced back-action optical trapping of dielectric
nanoparticles. *Nature Phys.* 5, 915-919 (2009).
32. Kang, J.-H. et al. Low-power nano-optical vortex trapping
via plasmonic diabolito nanoantennas. *Nature Commun.* 2,
582 (2011).
33. Tsai, W.-Y., Huang, J.-S., and Huang, C.-B., Selective
Trapping or Rotation of Isotropic Dielectric Microparticles
by Optical Near Field in a Plasmonic Archimedes Spiral.
Nano Lett. 14, 547-552 (2014).
34. Roxworthy, B. J., and Toussaint, K. C., Femtosecond-Pulsed
Plasmonic Nanotweezers. *Sci. Rep.* 2, 660 (2012).
35. Schwarz, F., Lörtscher, E., Break-junctions for Investigating
Transport at the Molecular Scale. *J. Phys. Condens. Matter.*,
26 (47), 474201 (2014).

36. Kim, Y., Song, H., Strigl, F., Pernau, H.-F., Lee, T., Scheer, E., Conductance and vibrational states of single-molecule junctions controlled by mechanical stretching and material variation. *Phys. Rev. Lett.*, 106 (19), 196804 (2011).
37. Zhang, W., Liu, H., Lu, J., Ni, L., Liu, H., Li, Q., Qiu, M., Xu, B., Lee, T., Zhao, Z., Atomic switches of metallic point contacts by plasmonic heating. *Light Sci. Appl.*, 8 (1), 1-8 (2019).
38. Gruber, C. M., Herrmann, L., Bellido, E. P., Dörssegger, J., Olziersky, A., Drechsler, U., Puebla-Hellmann, G., Botton, G. A., Novotny, L., Lörtscher, E., Resonant Optical Antennas with Atomic-Sized Tips and Tunable Gaps Achieved by Mechanical Actuation and Electrical Control. *Nano Lett.*, 20 (6), 4346-4353 (2020).
39. Park, H., Lim, A. K., Alivisatos, A. P., Park, J., McEuen, P. L., Fabrication of metallic electrodes with nanometer separation by electromigration. *Appl. Phys. Lett.*, 75 (2), 301-303 (1999).
40. Dubois, V., Raja, S. N., Gehring, P., Caneva, S., van der Zant, H. S. J., Niklaus, F., Stemme, G., Massively Parallel Fabrication of crack-defined gold break junctions featuring

- sub-3 nm gaps for molecular devices. Nat. Commun., 9, 3433 (2018).
41. Manjappa, M., Pitchappa, P., Singh, N., Wang, N., Zheludev, N. I., Lee, C., Singh, R., Reconfigurable MEMS Fano metasurfaces with multiple-input-output states for logic operations at terahertz frequencies. Nat. Commun., 9 (1), 1-10 (2018).
42. Xu, Z., Lin, Y. S., A Stretchable Terahertz Parabolic-Shaped Metamaterial. Adv. Opt. Mater., 7 (19), 1900379 (2019).
43. Hrtoň, M., Konečná, A., Horák, M., Šíkola, T., , and Křápek, V., Plasmonic Antennas with Electric, Magnetic, and Electromagnetic Hot Spots Based on Babinet's Principle. Phys. Rev. Appl., 13 (5), 054045 (2020).
44. Dreyhaupt, S. Winnerl, T. Dekorsy, and M. Helm, High-intensity terahertz radiation from a microstructured large-area photoconductor, Appl. Phys. Lett., 86 (12), 1-3 (2005).
45. Park, H. -R., Bahk, Y. -M., Choe, J. H., Han, S., Choi, S. S., Ahn, K. J., Park, N., Park, Q. -H., Kim, D. -S., Terahertz pinch harmonics enabled by single nano rods. Opt. Express, 19, 24775 (2011).

46. Park, H. -R., Bahk, Y. -M., Ahn, K. J., Park, Q. -H., Kim, D. -S., Martin-Moreno, L., Garcia-Vidal, F. J., Bravo Abad, J., Controlling terahertz radiation with nanoscale metal barriers embedded in nano slot antennas. *ACS Nano*, 5, 8340 (2011).
47. Strikwerda, A. C., Zalkovskij, M., Iwaszczuk, K., Lorenzen, D. L., Jepsen, P. U., Permanently reconfigured metamaterials due to terahertz induced mass transfer of gold. *Opt. Express*, 23, 11586 (2015).
48. Xu, B., Tao, N. J., Measurement of single-molecule resistance by repeated formation of molecular junctions. *Science*, 301 (5637), 1221-1223 (2003).
49. Laman, N., Harsha, S. S., Grischkowsky, D., Melinger, J. S., High-resolution waveguide THz spectroscopy of biological molecules. *Biophys. J.*, 94 (3), 1010-1020 (2008).
50. Nagai, N., Kumazawa, R., Fukasawa, R., Direct evidence of inter-molecular vibrations by THz spectroscopy. *Chem. Phys Lett.*, 413 (4-6), 495-500 (2005).
51. Heo, C., Ha, T., You, C., Huynh, T., Lim, H., Kim, J., Kesama, M. R., Lee, J., Kim, T.-T., Lee, Y. H., Identifying fibrillization

- state of A β Protein via near-field THz conductance measurement. ACS Nano, 14 (6), 6548-6558 (2020).
52. Png, G. M., Fischer, B. M., Appadoo, D., Plathe, R., Abbott, D., Double-layered Nitrocellulose Membrane Sample Holding Technique for THz and FIR Spectroscopic Measurements. Opt. Express, 23 (4), 4997-5013 (2015).
53. Liu, H. B., Chen, Y. Q., Zhang, X. C., Characterization of Anhydrous and Hydrated Pharmaceutical Materials with THz Time-domain Spectroscopy. J. Pharm. Sci-US, 96 (4), 927-934 (2007).
54. Xu, W., Xie, L., Zhu, J., Xu, X., Ye, Z., Wang, C., Ma, Y., Ying, Y., Gold nanoparticle-based terahertz metamaterial sensors: mechanisms and applications. ACS Photonics, 3 (12), 2308-2314 (2016).
55. Park, H. R., Ahn, K. J., Han, S., Bahk, Y. M., Park, N., Kim, D. S., Colossal Absorption of Molecules Inside Single Terahertz Nanoantennas. Nano Lett., 13 (4), 1782-1786 (2013).
56. Lee, S.-H., Lee, D., Choi, M. H., Son, J.-H., Seo, M., Highly sensitive and selective detection of steroid hormones using

- terahertz molecule-specific sensors. *Anal. Chem.*, 91 (10), 6844-6849 (2019).
57. Melinger, J. S., Laman, N., Grischkowsky, D., The underlying terahertz vibrational spectrum of explosives solids. *Appl. Phys. Lett.* 93. 011102 (2008).
58. Markelz, A. G., Roitberg, A., Heilweil, E. J., Pulsed terahertz spectroscopy of DNA, bovine serum albumin and collagen between 0.1 and 2.0 THz. *Chem. Phys. Lett.* 320, 42-48 (2000).
59. Taraskin, S. N. and Elliott, S. R., Nature of vibrational excitations in vitreous silica. *Phys. Rev. B.* 56. 8605-8622 (1997).
60. Shoji, T. and Tsuboi, Y., Plasmonic Optical Tweezers toward Molecular Manipulation: Tailoring Plasmonic Nanostructure, Light Source, and Resonant Trapping. *J. Phys. Chem. Lett.* 5, 2957-2967 (2014).
61. Righini, M. et al. Nano-optical Trapping of Rayleigh Particles and Escherichia coli Bacteria with Resonant Optical Antennas. *Nano Lett.* 9, 3387-3391 (2009).

62. Wang, K., Schonbrun, E., Steinvurzel, P., Crozier, K. B.,
Trapping and rotating nanoparticles using a plasmonic
nano-tweezer with an integrated heat sink. *Nature Commun.*
2, 469 (2011).
63. Juan, M. L., Gordon, R., Pang, Y., Eftekhari, F., Quidant, R.,
Self-induced back-action optical trapping of dielectric
nanoparticles. *Nature Phys.* 5, 915-919 (2009).
64. Kang, J. H., Kim, K., Ee, H. S., Lee, Y. H., Yoon, T. Y., Seo,
M. K., & Park, H. G., Low-power nano-optical vortex
trapping via plasmonic diabolos nanoantennas. *Nature*
Commun. 2, 582 (2011).
65. Tsai, W.-Y., Huang, J.-S., and Huang, C.-B., Selective
Trapping or Rotation of Isotropic Dielectric Microparticles
by Optical Near Field in a Plasmonic Archimedes Spiral.
Nano Lett. 14, 547-552 (2014).
66. Wei, M.-T., and Chiou, A., Three-dimensional tracking of
Brownian motion of a particle trapped in optical tweezers
with a pair of orthogonal tracking beams and the
determination of the associated optical force constants. *Opt.*
Express. 13, 5798-5806 (2005).

67. Roxworthy, B. J., Toussaint, K. C., Femtosecond-Pulsed Plasmonic Nanotweezers. *Sci. Rep.* 2, 660 (2012).
68. Dreyhaupt, S. Winnerl, T. Dekorsy, and M. Helm, High-intensity terahertz radiation from a microstructured large-area photoconductor, *Appl. Phys. Lett.* 86(12), 1–3 (2005).
69. A. Nahata, A. S. Weling, and T. F. Heinz, A wideband coherent terahertz spectroscopy system using optical rectification and electro-optic sampling, *Appl. Phys. Lett.* 69(16), 2321–2323 (1996)
70. Righini, M., Volpe, G., Girard, C., Petrov, D., and Quidant, R. Surface plasmon optical tweezers: tunable optical manipulation in the femtonewton range. *Phys. Rev. Lett.* 100, 186804 (2008).
71. Ashkin, A., Acceleration and Trapping of Particles by Radiation Pressure. *Phys. Rev. Lett.* 24, 156-159 (1970).
72. Ashkin, A., Dziedzic, J. M., Bjorkholm, J. E., and Chu, S., Observation of a single-beam gradient force optical trap for dielectric particles. *Opt. Lett.* 11, 288-290 (1986).
73. Neuman K.C. , and Block S. M. Optical trapping. *Rev. Sci. Instrum.* 75, 2787-2809 (2004).

74.Hajizadeh, F., and Reihani, S. N. S., Optimized optical trapping of gold nanoparticles., 18(2), 551-559 (2010).

국문초록

Connectivity-changing terahertz nanoantennas manipulated by mechanical bending and optical tweezing

Jiyeah Rhie

Department of Physics and Astronomy

The Graduate School

Seoul National University

금속 나노 미터 갭 구조를 가진 안테나는 금속 나노갭을 통해 퍼널링되는 전자기파의 증폭 및 국소적 집속을 제어하는 데 사용됩니다. 연구에 따르면 능동 안테나는 안테나 갭의 연결성을 변경하여 입사 전자기파의 진폭 및 공명 주파수와 같은 광학적 반응 중 하나를 조작합니다. 이 작업에서는 테라헤르츠 보우타이 안테나를 기반으로 갭의 연결성을 변경하고 테라헤르츠 스펙트럼에서 광학적 반응을 관찰했습니다. 먼저 유연한 기판을 바깥쪽으로 구부리면 디아볼로 어레이가 보타이 어레이로 금속연결성이 분리되는 테라헤르츠 안테나를 제작했습니다. 이 때, 테라헤르츠 스펙트럼상에서 공진 주파수는 보우타이 어레이로 변하면서 거의 2 배 값으로 주파수 변화를 보였습니다. 기판을 펴고/구부리고/다시 펼 때 전도도 측정의 전기적 특성과 테라헤르츠 투과 스펙트럼의 광학 특성을 분석하였습니다. 컨덕턴스 측정결과로는 디아볼로 안테나에서 전기적으로 연결되고 보타이 안테나에서 분리된 결과를 보여주었고 그에 따른 테라헤르츠 투과도에서는 공진 주파수가 2배 공진기처럼 주파수 이동을 보여줍니다. 이러한 특성 때문에 저는 안테나에 락토오스와 카페인 물질을 각각 떨어뜨렸습니다. 화학 물질의 흡수 피크와 공진 주파수가 일치할 경우, 화학적 감지 특성은 베어 기판의 드롭 캐스팅에 비해 감도와 선택

성이 증가합니다. 다른 한편으로, 저는 광학 트위징 방법으로 테라헤르츠 반사 스펙트럼에서 싱글 보타이 나노 갭에서 싱글 금 나노입자 검출 실험을 진행했습니다. 광학 트위징으로 싱글 입자를 안정적으로 조작하기 위한 조건을 찾고 트래핑 비디오로 분석하여 트래핑 퍼텐셜의 크기가 실온에서의 브라우니안 운동에너지($1 k_B T \sim 26 \text{ meV}$)보다 4 배 크다는 것을 확인했습니다. 테라헤르츠 반사도에서의 감소된 진폭은 테라 헤르츠 시간 영역 분광법에 의해 관찰되었고, 싱글 금 입자가 보타이 갭을 채웠다고 볼 수 있음을 시뮬레이션으로 확인했습니다. 이러한 작업들은 단일 또는 다중 생체 분자 검출의 사전 단계가 되어 응용연구에 밑거름이 될 것입니다.

Keywords: 테라헤르츠 시간 영역 분광법, 테라헤르츠 보타이 나노안테나, 플렉서블, 광학 트위징, 테라헤르츠파 변조, 분자 감지

Student Number: 2013-30119

List of Publications

1. Jiyeah Rhie, Sung Ju Hong, Dukhyung Lee, Dohee Lee, Hyeong Seok Yun, Young-Mi Bahk[‡], and Dai-Sik Kim[‡], “Two-fold Plasmonic Resonator Manipulated by Mechanical Bending for Terahertz Applications”, ACS Applied Nano Materials (under review)
2. Jiyeah Rhie [‡], Dukhyung Lee, Young-Mi Bahk, Jeeyoon Jeong, Geunchang Choi, Youjin Lee, Sunghwan Kim, Seunghun Hong, and Dai-Sik Kim. “Control of optical nanometer gap shapes made via standard lithography using atomic layer deposition”, Journal of Micro/Nanolithography, MEMS, and MOEMS 17(2), 023504 (2018)
3. Dasom Kim*, Hyeong Seok Yun*, Bamadev Das*, Jiyeah Rhie, Parinda Vasa, Young-Il Kim, Sung-hoon Choa, Namkyoo Park, Dukhyung Lee[‡], Young-Mi Bahk[‡], and Dai-Sik Kim[‡], “Topology-Changing Broadband Metamaterials Enabled by Closable Nanotrenches”, Nano Letters 21, 4202-4208 (2021)
4. Om Krishna Suwal, Jiyeah Rhie, Nayeon Kim, and Dai-Sik Kim[‡]. “Nonresonant 10^4 Terahertz Field Enhancement with 5-

nm Slits”, Scientific Reports 7, 45638 (2017)

5. Woongkyu Park, Jiyeah Rhie, Na Yeon Kim, Seunghun Hong & Dai-Sik Kim[‡]. “Sub-10 nm feature chromium photomasks for contact lithography patterning of square metal ring arrays”, Scientific Reports 6, 23823 (2016)

6. Young-Gyun Jeong*, Sanghoon Han*, Jiyeah Rhie, Ji-Soo Kyoung, Jae-Wook Choi, Namkyoo Park, Seunghun Hong, Bong-Jun Kim, Hyun-Tak Kim, and Dai-Sik Kim[‡]. “A Vanadium Dioxide Metamaterial Disengaged from Insulator-to-Metal Transition”, Nano Letters 15(10), 6318-6323 (2015)

7. Taehee Kang, Jiyeah Rhie, Joohyun Park, Young-Mi Bahk, Jae Sung Ahn, Hyeongtag Jeon and Dai-Sik Kim. “Resonance tuning of electric field enhancement of nanogaps”, Applied Physics Express 8, 092003 (2015)

8. Jeeyoon Jeong, Jiyeah Rhie, Woojin Jeon, Cheol Seong Hwang, Dai-Sik Kim[‡]. “High-throughput fabrication of infinitely long 10 nm slit arrays for terahertz applications”, Journal of Infrared, Millimeter, and Terahertz Waves 36, 262 (2015)

9. Nayeon Kim, Sungjun In, Dukhyung Lee[‡], Jiyeah Rhie,

Jeeyoon Jeong, Dai-Sik Kim[‡], and Namkyoo Park. “Colossal Terahertz Field Enhancement using Split-Ring Resonators with a Sub-10 nm Gap”, ACS Photonics 5 (2), 278–283 (2017)

10. Young-Mi Bahk, Sanghoon Han, Jiyeah Rhie, Joohyun Park, Hyeongtag Jeon, Namkyoo Park, and Dai-Sik Kim[‡]. “Ultimate terahertz field enhancement of single nanoslits”, Physical Review B 95, 075424 (2017)

11. Joon-Yeon Kim, Bong Joo Kang, Young-Mi Bahk, Yong Seung Kim, Joohyun Park, Won Tae Kim, Jiyeah Rhie, Sanghoon Han, Hyeongtag Jeon, Cheol-Hwan Park, Fabian Rotermund & Dai-Sik Kim[‡]. “Tunnelling current-voltage characteristics of Angstrom gaps measured with terahertz time-domain spectroscopy”, Scientific Reports 6, 29103 (2016)

12. Sanghoon Han, Joon-Yeon Kim, Taehee Kang, Young-Mi Bahk, Jiyeah Rhie, Bong Joo Kang, Yong Seung Kim, Joohyun Park, Won Tae Kim, Hyeongtag Jeon, Fabian Rotermund, and Dai-Sik Kim[‡]. “Colossal Terahertz Nonlinearity in Angstrom- and Nanometer-Sized Gaps”, ACS Photonics 3(8), 1440 (2016)

13. Kwanghee Lee, Jeeyoon Jeong, Young-Mi Bahk, Jiyeah

- Rhie, In-Keun Baek, Bong Jun Lee, Yu Hyun Kang, Seunghun Hong, Gun-Sik Park, and Dai-Sik Kim‡. “Microwave Funneling through Sub-10 nm Nanogaps”, ACS Photonics 3(4), 537 (2016)
14. Joon-Yeon Kim‡, Bong Joo Kang‡, Joohyun Park, Young-Mi Bahk, Won Tae Kim, Jiyeah Rhie, Hyeongtag Jeon, Fabian Rotermund, and Dai-Sik Kim. “Terahertz Quantum Plasmonics of Nanoslot Antennas in Nonlinear Regime”, Nano Letters 15(10), 6683-6688 (2015)
15. Young-Mi Bahk*, Bong Joo Kang*, Yong Seung Kim, Joon-Yeon Kim, Won Tae Kim, Tae Yun Kim, Taehee Kang, Jiyeah Rhie, Sanghoon Han, Cheol-Hwan Park, Fabian Rotermund‡, and Dai-Sik Kim‡. “Electromagnetic Saturation of Angstrom-Sized Quantum Barriers at Terahertz Frequencies”, Physical Review Letters 115, 125501 (2015)
16. Laxmi Narayan Tripathi, Taehee Kang, Young-Mi Bahk, Sanghoon Han, Geunchang Choi, Jiyeah Rhie, Jeeyoon Jeong, and Dai-Sik Kim‡. “Quantum dots-nanogap metamaterials fabrication by self-assembly lithography and photoluminescence studies”, Optics Express 23, 14937 (2015)

